Geophysical Journal International

Geophys. J. Int. (2019) **217,** 682–702
Advance Access publication 2019 January 21
GJI Geodynamics and tectonics

doi: 10.1093/gji/ggz040

Localized crustal deformation along the central North Anatolian Fault Zone revealed by joint inversion of *P*-receiver functions and *P*-wave polarizations

Christian Schiffer [1,2] Tuna Eken,[3] Stéphane Rondenay[4] and Tuncay Taymaz [3]

[1]*Department of Earth Sciences, Durham University, Science Site, DH*1 3*LE, Durham, UK. E-mail: christian.schiffer@zoho.com*
[2]*Department of Earth Sciences, Uppsala University,* 752 36 *Uppsala, Sweden*
[3]*Department of Geophysical Engineering, The Faculty of Mines, Istanbul Technical University, Maslak* 34469*, Istanbul, Turkey*
[4]*Department of Earth Science, University of Bergen, Allegaten* 41*, N-*5007 *Bergen, Norway*

Accepted 2019 January 17. Received 2018 December 17; in original form 2018 July 24

SUMMARY

The North Anatolian Fault Zone (NAFZ) is a major plate boundary that separates the Eurasian Plate to the north from the Anatolian Plate to the south and is associated with powerful damaging earthquakes. Despite numerous studies of the crust and upper mantle across the NAFZ, our understanding of the exact mechanisms and distribution of deformation with depth is still limited. Accurate models of the crustal velocity structure are key to assess seismic hazard associated with strike-slip deformation. Here, we address this need by employing a novel method that jointly inverts receiver function waveforms and *P*-wave polarizations to recover *S*-wave velocity structure from the surface to the upper mantle. The method is applied to a dense teleseismic data set collected across a segment of the central NAFZ in Turkey. The results provide important new constraints on the sedimentary thickness, depth to basement and Moho discontinuity beneath the region. Our estimates of uppermost sedimentary thickness range from 0 km in some areas (e.g. in the Central Pontides) to 6 km in the Çankırı Basin. Smaller basins are scattered along the NAFZ. A similar pattern is observed for the basement depth, with values exceeding 10 km beneath the Çankırı Basin, where the Moho is shallowest with a depth of ∼32 km. The Moho reaches a maximum depth of ∼42 km beneath the Central Pontides. Most other areas have an average Moho depth of 35–38 km. The results reveal clear structural–tectonic relationships in the crust: areas of fundamentally different sedimentary and crustal architecture are bounded by faults and suture zones. The NAFZ appears to accommodate small-scale basin and basement-highs, and acts as a thick-skinned (i.e. full crustal-scale) boundary between laterally displaced crustal blocks to the north and south. Seismicity clusters are centred on areas of low *Vp*/*Vs* ratios that may be representative of weak zones.

Key words: Composition and structure of the continental crust; Joint inversion; Body waves; Crustal imaging.

1 INTRODUCTION

Active continental fault zones have been the focus of extensive scientific attention owing to their seismic hazard potential. Continental strike-slip faults can reach lengths of hundreds of kilometres and may accommodate large deformation (Molnar & Dayem 2010). The deep structure of strike-slip fault zones and distribution of deformation is still a matter of debate. It is unclear whether shear zones remain narrow and localized in the lower crust and upper mantle or whether they expand into wide, distributed deformation bands at depths (Platt & Behr 2011), possibly accommodated by lower crustal ductile flow (Bürgmann & Dresen 2008). A key diagnostic is the presence or absence of a large and abrupt Moho response beneath a fault zone, which could hint at whether deformation is accommodated at depth via brittle or ductile behaviour, respectively (Zhu 2000; Weber *et al.* 2004; Wilson *et al.* 2004). Which process dominates, in turn, has important consequences on the distribution of seismicity along continental fault zones.

The North Anatolian Fault Zone (NAFZ) is a prominent example of an active continental strike-slip fault and forms an important part of the complex tectonic setting in the eastern Mediterranean and Anatolia. The recent tectonic evolution of this region is dominated by the Cenozoic closure of the Tethys Ocean and subsequent convergence of the Arabian and Eurasian plates. At the same time, the

African Plate converges and subducts northward beneath Anatolia along the Hellenic and Cyprus trenches (Dewey & Şengör 1979; Taymaz *et al.* 1991, 2007b; Schildgen *et al.* 2014). GPS measurements (Reilinger *et al.* 2006) indicate that slab rollback of the subducting African lithosphere could have a major effect on the rapid deformation of Anatolia. The NAFZ, a right-lateral (dextral) fault system of Miocene age, forms the boundary between the Anatolian Plate to the south and the Eurasian Plate to the north (Barka 1992; Şengör *et al.* 2005; Le Pichon *et al.* 2015). It stretches over 1600 km across Anatolia and has generated several destructive earthquakes in the 20th century (Şengör *et al.* 2005).

This work aims to elucidate the origin of seismic velocity contrasts in the crust and uppermost mantle along the central NAFZ using joint inversion of *P*-receiver functions and *P*-wave polarization data. Several suture zones and tectonic boundaries are located across Anatolia, bearing witness of the complex tectonic history involving successive accretion and collision events, that is the Intra-Pontide and Izmir-Ankara-Erzincan Suture Zones (IAESZ), the Istanbul Zone, the Sakarya Zone, the Central Pontides, the Kırşehir Massif, the Ezine Pazari-Sungurlu Fault and the Çankırı Basin (Kaymakçı *et al.* 2003, 2009, Fig. 1). The Pontides in the north of the study area belong to the Sakarya Continent terrane. The Kırşehir Block, as the northern continuation of the metamorphic Anatolides, is located to the south of the study area (Şengör & Yılmaz 1981). The Çankırı Basin lies above the east–west trending IAESZ between the Pontides to the north and the Kırşehir Block to the south (Kaymakçı *et al.* 2003) (Fig. 1). Kaymakçı (2000) propose that the Çankırı Basin was formed from Late Cretaceous to Early Miocene times in response to the collision and indentation of the Sakarya Continent and the Kırşehir Block. The sedimentary infill of this basin has a thickness of more than 4 km, with sediment ages ranging from Late Cretaceous to present. Information on the crustal seismic velocity structure across this region will provide new insight into the distribution of the different crustal blocks and weak zones at depth, and their possible link to seismicity along the NAFZ.

2 PREVIOUS SEISMOLOGICAL WORK

The NAFZ has been subject to several seismic experiments, the data from which have been analysed using a variety of methods. In the early 2000s, relationships between seismicity and crustal velocity structure beneath the NAFZ were investigated by local earthquake tomography (Nakamura *et al.* 2002; Yolsal-Çevikbilen *et al.* 2012; Polat *et al.* 2016; Çubuk-Sabuncu *et al.* 2017) and active-source seismic tomography (e.g. Karabulut *et al.* 2003; Bayrakci *et al.* 2013) in the Marmara Sea region. Gans *et al.* (2009) interpreted regional Pn velocity anomalies as evidence for slab break-off under Anatolia. Koulakov *et al.* (2010) presented a regional tomography model showing that the crust in the western NAFZ is characterized by low *Vp* and *Vs*, and high *Vp*/*Vs* ratios. Recently, full-waveform tomography of the crust in western Anatolia by Çubuk-Sabuncu *et al.* (2017) confirmed these results. Seismic activity, as an indicator of ongoing deformation within the crust, has been shown to occur not only along the main branch of the NAFZ but also to extend to the south. (see Taymaz *et al.* 2007a for the 2000 Orta earthquake, Çubuk-Sabuncu *et al.* 2014 for the 2005 and 2008 Bala-Sırapınar earthquakes; Karasözen *et al.* 2013).

In the last decade, two dense temporary seismic arrays were deployed across the western and central NAFZ. These new stations allowed for local high-resolution seismic analyses and expanded the data coverage for regional seismological models. Yolsal-Çevikbilen *et al.* (2012) imaged small-scale *Vp*/*Vs* variations in the crust of the central NAFZ and identified high-velocity blocks in the mid to lower crust that appear to be dissected by suture zones. Using ambient noise tomography, Warren *et al.* (2013) imaged the crust of central and eastern Anatolia. They found that most crustal velocity variations could be attributed to tectonic boundaries and suture zones. However, they did not detect robust correlations between velocities and the NAFZ, consistent with the results of Yolsal-Çevikbilen *et al.* (2012). The receiver function results of Kahraman *et al.* (2015) do not show evidence of large Moho variations in response to the western NAFZ, but they contain signals indicative of rheological differences across the fault zone reaching into the upper mantle. In contrast, autocorrelation of ambient seismic noise suggests a substantial Moho offset related to the northern branch of the NAFZ in the same region, while no such offset is observed on the southern branch (Taylor *et al.* 2016). Polat *et al.* (2016) carried out local *P*- and *S*-wave tomography to image 3-D seismic velocity variations across different branches of the NAFZ in the Marmara Sea region. They found that high-velocity anomalies appear to be coincident with the rupturing segments of the NAFZ where most of the observed high seismicity is concentrated. Papaleo *et al.* (2017, 2018) imaged the lithosphere of the western NAFZ using teleseismic tomography and identified substantial *P*- and *S*-velocity variations along- as well as across-strike the various branches of the NAFZ. Licciardi *et al.* (2018) investigated the anisotropy in the central NAFZ based on azimuthal variations of receiver functions and found that the NAFZ divides a crustal block of relatively weak and homogeneously oriented anisotropy to the north from a highly and heterogeneously anisotropic block to the south, with the strongest anisotropy in the upper 15 km of the crust.

A number of regional-scale seismic studies have been carried out with combined data sets from nationwide networks of permanent stations and local temporary arrays. Here we briefly discuss three of these studies whose results are relevant to this work. Firstly, a recent full-waveform tomography study was performed over the entire Anatolian Plate by Fichtner *et al.* (2013a, b). Their results suggest that *Vs* structure in the mid/lower crust and uppermost mantle correlates with both the NAFZ and suture zones in the region. These authors interpreted the NAFZ as a Tethyan suture zone representing a transition from a broad zone of weakness in the upper mantle to a narrower focussed deformation zone in the rigid blocks of the crust. Secondly, Moho depths beneath the entire Anatolian Plate were obtained from receiver function analysis by Vanacore *et al.* (2013). Their model implies that small-scale fragments of thinned crust (i.e. shallow Moho) appear to be dissected by the NAFZ. Thirdly, a regional ambient noise tomography by Delph *et al.* (2015) inferred a clear relationship between suture zones and velocity anomalies across Anatolia, but only a weak link between the NAFZ and velocity anomalies.

Although these previous seismic studies have provided important insight into the interplay between lithospheric structure and the NAFZ, they have not yet succeeded in providing a coherent picture of how deformation is distributed with depth along the entire fault. This may be due to the fact that different methods have inherently varying sensitivities and resolutions that produce contrasting images of the same general crust-upper mantle structure along the NAFZ. Alternatively, the structural variations are real and reflect differences in rheological properties and style of deformation along the fault zone. We shall contribute new insight to this critical discussion by applying a novel joint inversion of *P*-receiver functions and *P*-wave polarization to a large natural-source seismic data set collected across the central NAFZ.

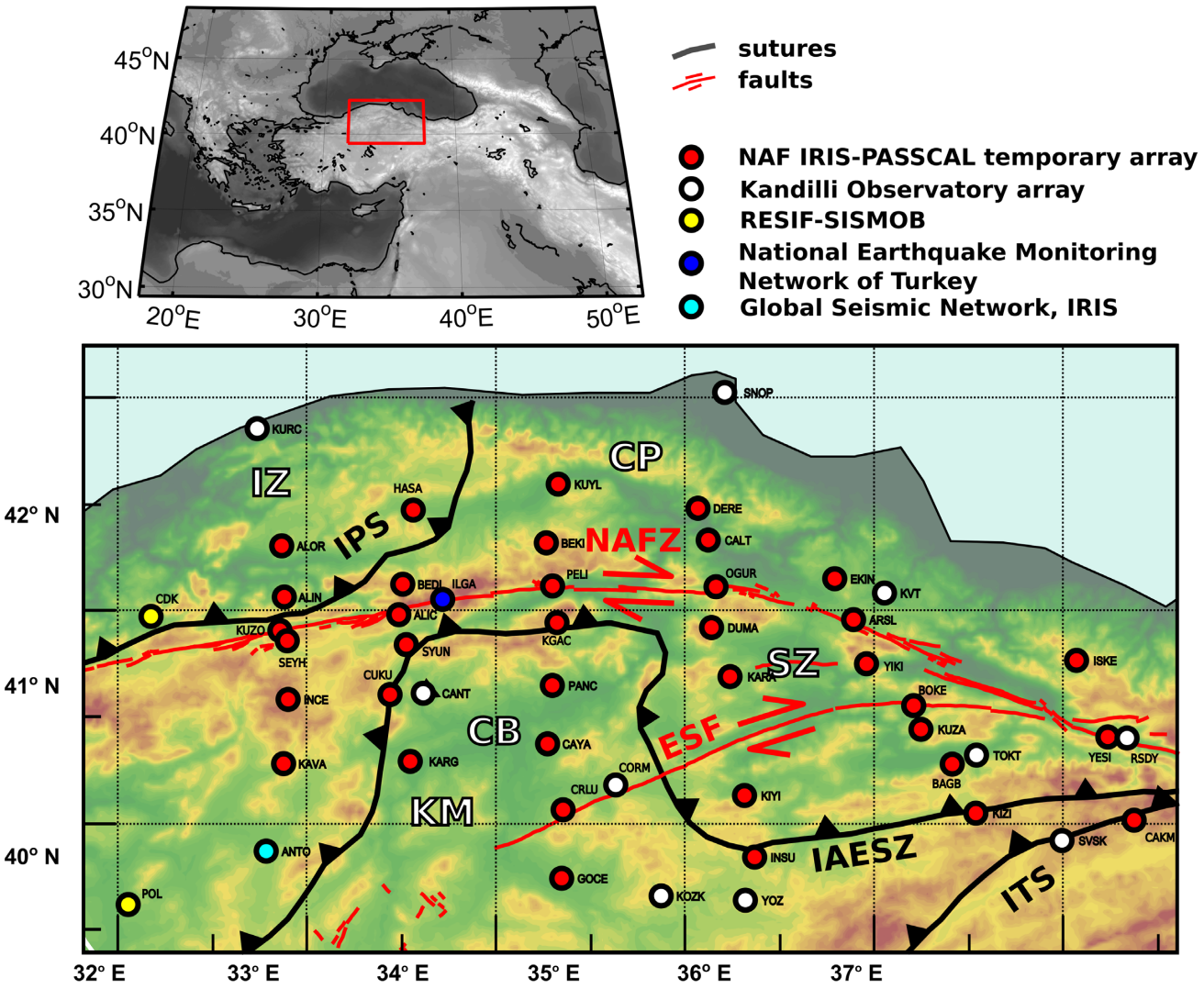

Figure 1. Outline of the study area within the broader eastern Mediterranean region (above) and closeup (lower panel), with topography from ETOPO1 (Amante & Eakins 2009). Major faults are indicated in red. Suture zones, modified after Kaymakçı *et al.* (2003), are shown in grey. CB, Çankırı Basin; CP, Central Pontides; ESF, Ezinepazari-Sungurlu Fault; IAESZ, Izmir-Ankara-Erzincan Suture Zone; IPS, Intra-Pontide Suture; IZ, Istanbul Zone; ITS, Intra-Tauride Suture; KM, Kırşehir Massif; NAF, North Anatolian Fault; SZ, Sakarya Zone.

3 DATA

In this study, we analysed three-component teleseismic waveform data extracted from continuous recordings that were acquired between January 2006 and May 2008 at 38 broad-band seismic stations within the framework of the North Anatolian Fault (*NAF*) passive seismic experiment (Biryol *et al.* 2010). For each station, we selected the events with high signal-to-noise ratio waveforms using a visual inspection process. These waveforms were extracted from a list of about 1000 teleseismic events with magnitudes $\geq$5.5 that occurred at epicentral distances (Δ) between 30° and 100°. Most of the events originate from the first quadrant for the selected Δ range, corresponding to the major circum-Pacific seismogenic zones (Fig. 2). Additionally, we used similar teleseismic data from 14 stations belonging to different seismic networks deployed in the study area (see Table 1)—these data were downloaded through *ORFEUS* (http://www.orfeus-eu.org/). Eleven other stations from *ORFEUS*, as well as station *DOGL* of the *NAF* were disregarded due to incomplete waveforms, poor data quality or apparent timing problems. Station *DOGL* recorded a sufficient number of good events, but the signals lack *P*-wave energy on the radial component (no significant signal at 0 s, see Supplementary File S1). The absence of *P*-wave energy on the radial component of a seismogram indicates a near-vertical apparent incident angle that translates into unrealistically low apparent velocities. *DOGL* is located directly atop the ESF, where strong scattering and boundary effects, as well as heavily fractured bedrock are expected and may obscure the signal. As we do not have additional information that could help mitigate this peculiar behaviour at *DOGL*, we decided to disregard the station entirely. The spatial distribution of the 51 stations ultimately used in our analysis is shown in Fig. 1. An overview of station names, locations, network and number of processed events for all these stations can be found in Table 1. Further details about the earthquakes used in this study are provided in Supplementary File S2.

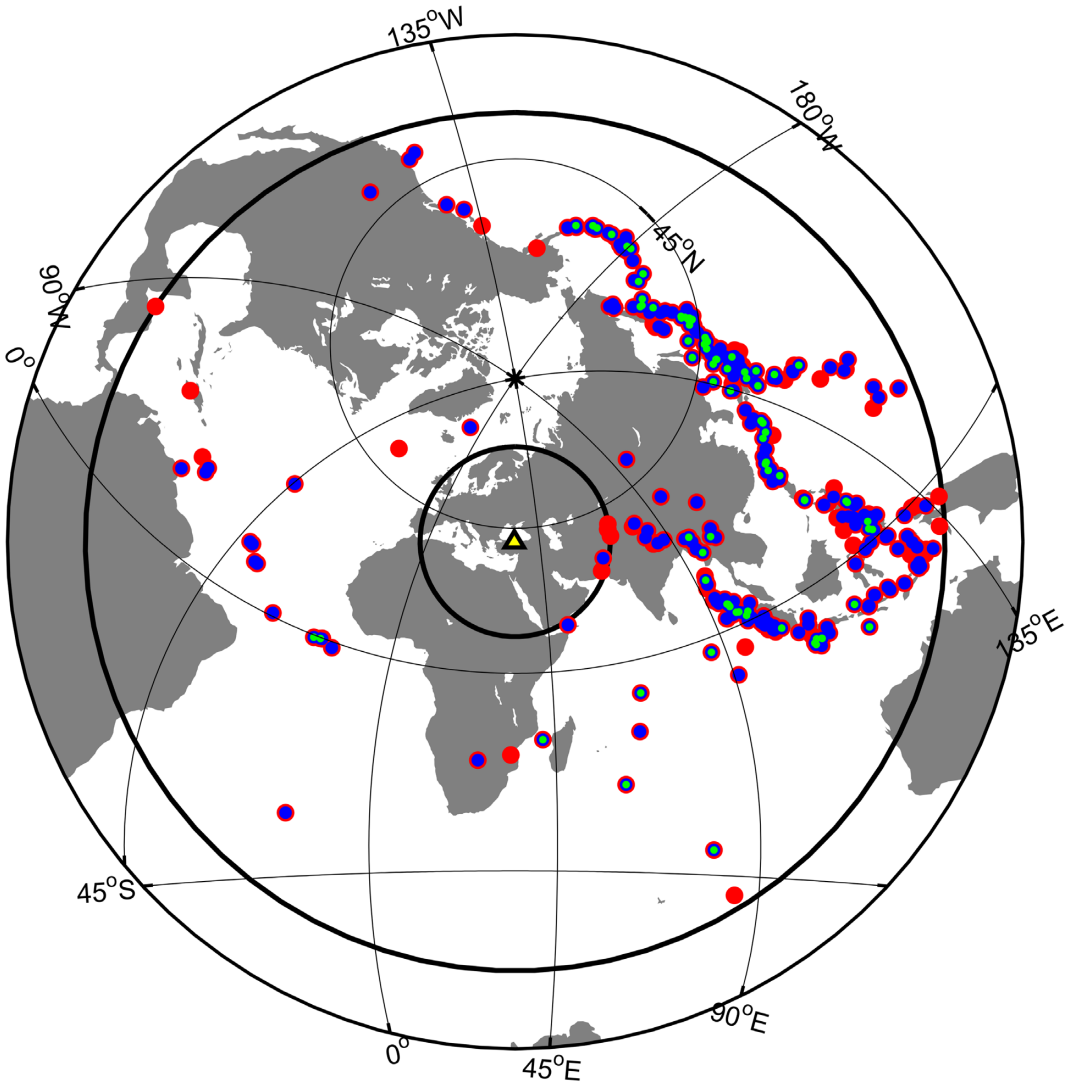

Figure 2. Distribution of all the teleseismic events used in this study. The map is centred on the geographical centroid of the seismic network (yellow triangle). The thick black circle marks epicentral distances of 30° (inner circle) and 100° (outer circle). Red dots are events of magnitude ≥7, blue dots are earthquakes of magnitude between 6 and 7, and green dots are all earthquakes with a magnitude <6. A detailed list of all the earthquakes used in our analysis is provided in Supplementary File S2.

4 RECEIVER FUNCTION AND Vs_{app} INVERSION

Our inversion method employs two data sources as inputs: *P*-receiver functions and *P*-wave polarizations. The first data source, *P*-receiver functions (RFs), provide estimates of the grounds' impulse response by deconvolving the incident wavefield from the converted wavefield (Rondenay 2009). Here, we generate receiver functions by applying water-level deconvolution (Clayton & Wiggins 1976; Langston 1979; Ammon 1991) to the waveforms of recorded P-to-S (Ps) converted teleseismic earthquakes. On its own, RF inversion is already a widely used and well-established technique to obtain quantitative information on the lithospheric velocity structure from these deconvolved conversions (Owens *et al.* 1987; Ammon *et al.* 1990; Cassidy & Ellis 1993; Sandvol *et al.* 1998; Darbyshire 2003; Ottemöller & Midzi 2003). The second data source, the polarization of incident *P* waves, provides insight into the absolute *S*-wave velocity distribution in the shallow subsurface within a homogeneous medium (Wiechert & Zoeppritz 1907). This *P*-wave polarization information is contained in the ratio of the radial (R) to the vertical (Z) RFs, that is R-RF/Z-RF, at zero delay time (Svenningsen & Jacobsen 2007). If the velocity changes with depth, then the polarization now reflects an apparent *S*-wave velocity (Vs_{app}), which integrates the velocities over the entire depth range covered by the dominant wavelength of the signal. A set of apparent *S*-wave velocities computed from different wavelengths can then be inverted to recover the absolute velocity model. Here, we estimate the vertical apparent *S*-wave velocity distribution by computing the R-RF/Z-RF ratio at increasing periods (T), following the procedure by Svenningsen & Jacobsen (2007). This principle has recently been applied to both onshore and offshore studies (Schiffer *et al.* 2015, 2016; Hannemann *et al.* 2016; Chong *et al.* 2018). Each individual RF is used to calculate distinct $Vs_{app}(T)$ curves, while the median curve is considered to give the most robust representation. T is defined as 26 values on a logarithmic scale from 1 to 25 s. The data error is defined as the standard deviation of the 68 per cent $Vs_{app}(T)$ curves closest to the mean.

Table 1. Station information.

Station	Latitude	Longitude	Array	No. events	Station	Latitude	Longitude	Array	No. events
ALIC	40.978	33.487	NAF	47	KIZI	40.048	36.536	NAF	37
ALIN	41.061	32.879	NAF	54	KUYL	41.59	34.332	NAF	73
ALOR	41.301	32.87	NAF	40	KUZA	40.441	36.248	NAF	85
ARSL	40.955	35.887	NAF	28	KUZO	40.904	32.861	NAF	81
BAGB	40.278	36.41	NAF	65	OGUR	41.109	35.165	NAF	65
BEDI	41.121	33.506	NAF	56	PANC	40.647	34.301	NAF	67
BEKI	41.315	34.263	NAF	62	PELI	41.113	34.299	NAF	73
BOKE	40.552	36.211	NAF	19	SEYH	40.856	32.9	NAF	70
CAKM	40.015	37.367	NAF	60	SYUN	40.838	33.529	NAF	98
CALT	41.328	35.125	NAF	57	YESI	40.405	37.229	NAF	21
CAYA	40.373	34.269	NAF	20	YIKI	40.748	35.954	NAF	52
CRLU	40.064	34.357	NAF	40	ANT	39.87	32.79	GSN	51
CUKU	40.604	33.441	NAF	31	CANT	40.61	33.62	KO	27
DERE	41.477	35.064	NAF	33	CDK	40.97	32.18	RS	51
DUMA	40.918	35.14	NAF	51	CORM	40.18	34.63	KO	78
EKIN	41.147	35.787	NAF	22	ILGA	41.05	33.72	TU	34
GOCE	39.743	34.348	NAF	113	KOZK	39.66	34.87	KO	29
HASA	41.469	33.565	NAF	72	KURC	41.85	32.74	KO	29
INCE	40.581	32.906	NAF	61	KVT	41.08	36.05	KO	24
INSU	39.842	35.366	NAF	39	POL	39.62	32.06	RS	31
ISKE	40.764	37.067	NAF	18	RSDY	40.4	37.33	KO	8
KARA	40.688	35.245	NAF	49	SNOP	42.02	35.21	KO	29
KARG	40.291	33.552	NAF	8	SVSK	39.92	36.99	KO	22
KAVA	40.28	32.878	NAF	12	TOKT	40.32	36.54	KO	67
KGAC	40.941	34.323	NAF	52	YOZ	39.64	35.32	KO	37
KIYI	40.131	35.316	NAF	48					

NAF, North Anatolian Fault Zone array (https://doi.org/10.7914/SN/YL_2005); GSN, Global Seismic Network (https://doi.org/10.7914/SN/II) ; KO, Kandilli Observatory & Earthquake Research Institute (https://doi.org/10.7914/SN/KO) ; RS, RESIF-SISMOB (https://doi.org/10.15778/RESIF.XY2007); TU, National Seismic Network of Turkey.

We jointly invert Vs_{app} curves and RF waveforms using a linearized inverse procedure (Tarantola & Valette 1982; Menke 1989; Ammon *et al.* 1990) based on to the approaches presented in Schiffer *et al.* (2015) and Schiffer *et al.* (2016). The RFs are modelled from –1 to 20 s delay time and Vs_{app} from 0 to 25 s periods. The non-uniqueness of the inverse problem is reduced by parametrizing layers in delay-time instead of thickness (Jacobsen & Svenningsen 2008). The inversion is adjusted to primarily fit the $Vs_{app}(T)$ curves by weighting these by a factor of 2 compared to the RF waveforms. The inclusion of RF waveforms in the inversion helps retaining the sensitivity to sharp velocity discontinuities, which is otherwise lost when only inverting $Vs_{app}(T)$. *Vp* values were determined on the basis of Poisson's ratios between 0.25 and 0.3 for various lithologies (Christensen 1996) and densities are calculated from *Vp* at different depth (Christensen & Mooney 1995). The inversion is thereby not technically inverting for *Vp* as an independent parameter, but the best-fitting *Vs–Vp* combination is estimated following the predefined lithology-dependent *Vp*/*Vs* ratios. We can therefore use the resulting *Vp*/*Vs* ratios for interpretation. *A priori* data errors based on the independent data covariance matrices are used to automatically weigh the individual data sets. That is, if one data set shows a larger spread, the observed error is large and the weight of the respective data set is reduced in the inversion. Data and model uncertainties are thoroughly discussed in Section 6.1.

Fig. 3 shows examples of RFs and Vs_{app} curves for two stations with different number of events, for comparison—*ALIC* (Fig. 3a) has a large number of events, whereas *KOZK* (Fig. 3b) has a smaller number of events. The reduced data set at *KOZK* leads to a much larger observed data error compared to *ALIC*. Corresponding figures from all other stations are documented in Supplementary File S3. The Vs_{app}-method is only stable for frequencies contained in the original recorded waveforms. Hence, in our case, the original waveforms must contain frequencies down to at least $T^{-1} = 0.04$ Hz ($T = 25$ s).

Examples of the progression of the inversion at these two stations are shown in Fig. 4, and corresponding figures for all other stations are shown in Supplementary File S4. Starting models and observed data are represented by black lines, whereas each iteration of the linearized inverse model is colour coded with blue-green-yellow-orange-red colours representing early-to-late iterations and the last iteration is always denoted in red. The bottom left-hand panel shows the evolution of the data error though the various iterations. The error is usually reduced at each iteration of the inversion, which ends when the models and errors converge, that is changes of less than 1 per cent are observed for more than two iterations (see details in the figure caption). The starting models comprise three major discontinuities at mid-crustal and Moho depths to reflect the largest peaks observed in the RFs, and an additional layer boundary in the upper mantle to allow for sub-Moho structure. Three thin layers with 0.2, 0.3 and 0.5 s delay time are also defined at the top of the model to adequately constrain sedimentary basins. The uppermost velocities of the starting model are set to fulfil the first three values of the $Vs_{app}(T)$ curves, respectively. Velocities and depths/delay times are virtually unconstrained in the inversion, meaning that both model parameters can freely change without causing a large model error. There are two exceptions to this rule: (1) the uppermost *S*-wave velocity, which is more tightly constrained to the first $Vs_{app}(T = 1$ s) by an *a priori* standard deviation of 0.2 km s^{-1} and (2) the lowermost mantle half-space velocity, which is tied to a velocity of $Vs = 4.6$ km s^{-1} by an *a priori* model error of 0.2 km s^{-1}. The final model is defined by the average of the last 10 model iterations.

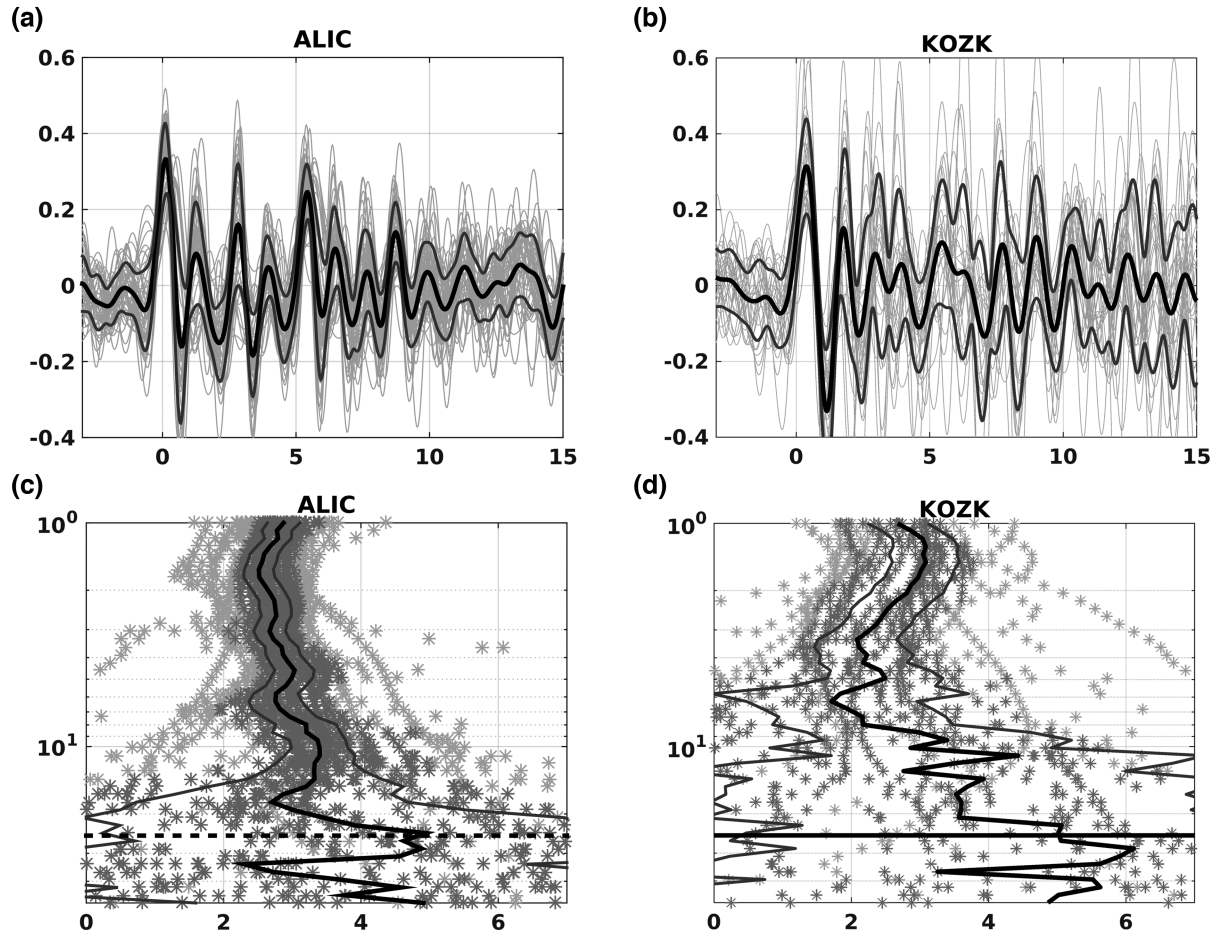

Figure 3. Examples of receiver function (a,b) and Vs_{app} (c,d) for a seismic station of high quality (ALIC, a, c) and lower quality (KOZK, b,d). The receiver function stack is shown as a thick black line, with the standard deviation in dark grey. All individual receiver functions are plotted in light grey in the background. The median Vs_{app} curves are shown in black, with the standard deviation in dark grey. Individual Vs_{app} values are shown as grey stars, with those within 68 per cent confidence interval around the median shown in darker grey. The horizontal stippled black line indicates the limit of 25 s used for the inversion.

We perform a number of synthetic tests to evaluate the performance of the inversion. A detailed description and documentation of the different model setups, the progression of the inversions and inversion results are shown in Supplementary File S5. We define four hypothetical crustal reference models on top of a mantle half space: (i) A two-layered crystalline crust (20 km of upper and lower crust), (ii) the same model with the addition of two sedimentary layers of 1.5 and 3.5 km thickness replacing the uppermost crystalline crust, (iii) the same model as (i) with a 5 km thick high velocity lower crustal layer and, finally, (iv) the combination of models (ii) and (iii) with two sedimentary layers and high velocity lower crust. We use the same ray-geometries as those for the events recorded at station *ALIC*, taking into account variations in ray-parameters and associated changes in *P*-wave amplitude at $t = 0$ s and the delay times of primary and multiple conversions. We apply exactly the same inverse algorithm as that described above in this section to the synthetic data, without any *a priori* model information. Four tests are performed for each of the reference models. (a) An average of 1 per cent random velocity and layer depth perturbations are added to the velocity model before calculating each the 47 synthetic waveforms. This allows us to approximate the effects of ambient geological changes in the vicinity of the station. (b) The same setup as for (a), with the addition of realistic seismic noise captured in a random time window preceding the *P*-arrivals in the real data recorded at station *ALIC*. (c) The same test as described in (a) with 5 per cent model perturbations. (d) The same test as described in (c) with additional noise from the observed receiver function. We perform four additional tests to explore the role of velocities in the starting models: The structurally most complex models with most and least perturbation and noise are inverted with a constant mantle velocity; another is performed with a constant crustal velocity on top of the mantle half space.

In all tests, the crustal velocity structure is well recovered. However, the data and recovered velocity models show larger misfits with added noise and increasing geological variation, as is to be expected. Geological variations appear to create smoother primary conversions and even smoother multiple conversions, which replicate apparent velocity gradients rather than sharp discontinuities. Because of the intentional minimal setup of our models, these apparent gradients cannot be fully recovered. However, it can be observed that the interfaces are modelled using a step if the model setup allows for such structure and an additional layer is available, for example for the Moho and other known interfaces. In summary, our synthetic tests reveal that the overall model recovery is very good despite the presence geological variations and noise, and that our inverse approach can thus be deemed robust.

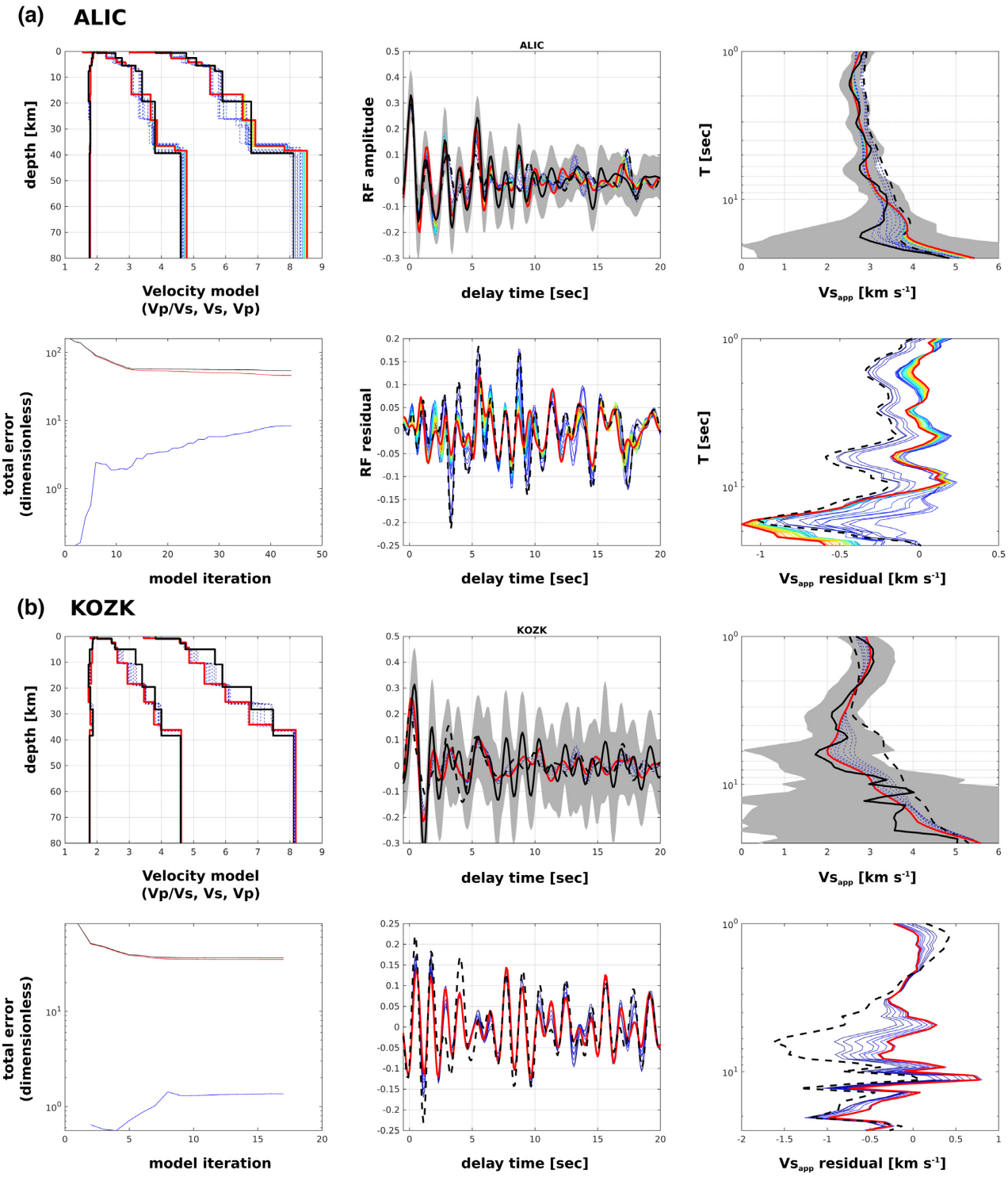

Figure 4. Examples of receiver function-Vs_{app} inversion results for a high-quality station (ALIC, a) and a lower-quality station (KOZK, b). Different colours indicate the progression of the inversion in each panel. Blue colours denote early iterations, whereas reds denote later iterations. Since the inversion is stopped as soon as the inversion converges towards a constant model, not all models reach the maximum number of iterations of 50. The last iteration is shown by the thick red line in all plots. Upper left: The starting velocity model is denoted by a solid black line. Upper middle: Iterations over the receiver functions fit, with the solid black line representing the observed receiver function, the dashed black line denoting the RF for the starting model and the red thick line denoting the RF for the model of the last iteration. The grey shading marks the standard deviation at each receiver function time step. Upper right: Iterations over the Vs_{app} curve fits, with the solid black line representing the observed Vs_{app}, the dashed black line denoting the Vs_{app} for the starting model and the red line denoting the Vs_{app} for the model of the last iteration. The grey shading marks the standard deviation at each period of the Vs_{app} curve. Lower left: development of the inversion error at each iteration, with the total error in black, the data error (receiver functions and Vs_{app}) in red and the model error in blue. Lower middle: Residual receiver function for each iteration. Stippled black line denotes the starting model and the solid red line the model of the last iteration. Lower right: Residual Vs_{app} curve for each iteration. Stippled black line denotes the starting model and the solid red line the model of the last iteration.

5 RESULTS

The final inversion results for the stations that we have used as examples in Section 4, *ALIC* and *KOZK*, are shown in Fig. 5. Those for all other stations are presented in Supplementary File S6. The 1-D model results are integrated and displayed as maps showing average *Vs* over the 0–5 km and 5–15 km depth ranges, and average *Vp*/*Vs* ratio in the top 15 km of the study area (Section 5.1, Figs 6 and 7). All maps are produced using kriging of every individual station results using the MATLAB kriging toolbox, DACE (Lophaven *et al.* 2002). In the rest of the section, we interpret the *Vs* models in terms of (i) thickness of the sedimentary cover (Section 5.2), (ii) depth to crystalline basement (excluding metasediments) (Section 5.2), and (iii) depth to Moho (Section 4.3). These three interfaces are defined according to velocity discontinuities that exceed certain thresholds in *Vs*. The sedimentary thickness is defined by the shallowest discontinuity that exceeds $Vs = 2.5$ km s^{-1}. The depth to the crystalline basement interface is defined as the shallowest discontinuity at which $Vs = 3.05$ km s^{-1} is exceeded. Basement depth is different from the sedimentary thickness, as we assume that possible metasediments are not part of the sedimentary succession, while basement depth does include these. The Moho is defined as the average depth of all model-discontinuities that lie in the range of *Vs* from 4.05 to 4.6 km s^{-1}.

We are aware of the uncertainties of the inverse approach and the fact that different lithologies can have overlapping velocities. In particular, fracturing of crystalline rocks can reduce *S*-wave velocities to values approaching those of sediments, an effect that may be important in a highly deformed study area such as the NAFZ. Additionally, seismic anisotropy related to fracturing, strike-slip deformation, metamorphism or intrusions may have a large impact on the measured velocities, depending on the primary orientation of incoming earthquake waves (Fouch & Rondenay 2006). This may lead to errors in the interpretation.

To put our inversion results in a regional context, we display them in map view in Fig. 8 and along five N–S oriented profiles in Fig. 9. And to link back to the input data, Fig. 10 displays the receiver function waveforms on the same five profiles, along with the interpreted interfaces from Fig. 9. It is usually difficult to identify clear phases for the sedimentary layers and basement interface in the receiver functions of Fig. 10, as these signals interact with the primary *P*-wave and sedimentary multiples, and form complex interferences. For most stations, the interpreted Moho corresponds to a clear positive pulse in the receiver functions. However, at a few stations the Moho signal is either weak or absent. This deterioration of the Moho signal likely stems from destructive interference with sedimentary or intra-crustal multiples. This effect might be amplified when the Moho is gradational or characterized by a small velocity discontinuity, for example when a high-velocity lower crust is present.

5.1 Crustal velocity structure

Clear variations in *Vs* can be observed in the 0–5 km depth range (Fig. 6a). Three areas of consistently high or low velocities are identified: (i) In the Çankırı Basin and Kırşehir Block, the uppermost *Vs* are generally low (1.9–2.2 km s^{-1}), with few exceptions (*CORM, YOZ*); (ii) the northwest of the study area (Istanbul Zone and Central Pontides, ∼41.5°N, ∼32.5–34.5°E) exhibits higher *Vs* (2.7–3.1 km s^{-1}); and (iii) the area between NAFZ/ESF and the IAESZ, in the central-eastern part of the study area, also exhibits higher *Vs* (stations *KUZA, BAGB, TOKT, YESI*). All other areas have moderate *Vs* variations (∼2.2–2.7 km s^{-1}) on smaller scale (small wavelength), which may reflect the natural geological variation in the study area including minor undulating basins and transitions between different terranes or levels of fracturing and faulting. The velocity variation in the 0–5 km depth range is particularly indicative of the presence or absence of sedimentary layers. For example, the Çankırı Basin is clearly outlined by low velocities (Fig. 6a). Conversely, high *Vs* represent areas without significant sedimentary cover and basement highs, such as the Istanbul Zone and the Central Pontides.

Vs in the 5–15 km depth range may still be affected by very deep sedimentary basins, but mainly represent variations in seismic properties, compositions and fabrics of the upper-middle crystalline crust (Fig. 6b). The lateral distribution of *Vs* between 5–15 km depth shows variations at much larger wavelength compared to the shallow layers. The Çankırı Basin and Kırşehir Massif are still characterized by relatively low *Vs* (2.5–3 km s^{-1}), which may indicate the presence of deep basin structure (>5 km) beneath the Çankırı Basin, and the presence of metasediments in the Kırşehir Massif. All other areas are characterized by *Vs* of > 3 km s^{-1}, with the exception of a few isolated stations (*KVT, SVSK, KUZO*).

The *Vp*/*Vs* ratios across the study area show clear variations ranging from approximately 1.73–1.85 (Fig. 7). High *Vp*/*Vs* ratios are observed in the Çankırı Basin, in the southeast of the study area and at a few stations located above the NAFZ. Low values are found for areas of high topography and no or little sedimentary cover, in the northwest (Istanbul Zone), central north (Central Pontides) and central west (Sakarya Zone and the area bound by the IAEFZ and NAFZ). Though we shall further discuss these results in the next sections, we must remind the reader that they have some limitations, as *Vp* is not a proper inversion parameter. Instead, *Vp*/*Vs* ratios are defined as a function of *Vs*. Still, the inversion estimates the optimal *Vs*–*Vp* combination as a function of depth beneath each station.

5.2 Sedimentary thickness and basement depth

The interpreted sedimentary thickness (Fig. 8a) roughly mimics the map of *Vs* in the 0–5 km depth range (Fig. 6a). The deepest and largest basin is estimated in the area of the Çankırı Basin (stations *CANT, PANC, KARG, CAYA, CRLU*), with up to 6 km of sedimentary rocks. Another deep but spatially quite confined basin is inferred above and to the north of the NAFZ in the western part of the study area (stations *KUZO* and *ALIN*). Another small area of thicker sedimentary cover is found around station *OGUR* located on top of the NAFZ in the centre of the study area. Thin sedimentary cover (<1 km) is inferred across the northwest (Istanbul Zone), central-north (Central Pontides) and southeast regions of the study area, whilst all other areas indicate moderate thicknesses of 1–3 km.

The depth to crystalline basement map (Fig. 8b) shows a slightly different pattern compared to the sedimentary thicknesses (Fig. 8a). Crystalline basement generally lies deep (>8 km) in most of the Çankırı Basin (*CUKU, CANT, KARG, PANC, CRLU, GOCE, KOZK*), but some stations indicate shallower basement (∼5 km at *CAYA* and *CORM*). In the southern part of the Çankırı Basin, the sedimentary layer has been estimated to be only 1–3 km thick at locations where the basement is >8 km deep (*CRLU, GOCE, KOZK*), suggesting that a 5–7-km-thick metasedimentary layer or heavily fractured uppermost crystalline crust may exist beneath this region. This also applies to a group of stations close to the NAFZ in the west of the study area (*SEYH, INCE*) and in the southeast of the

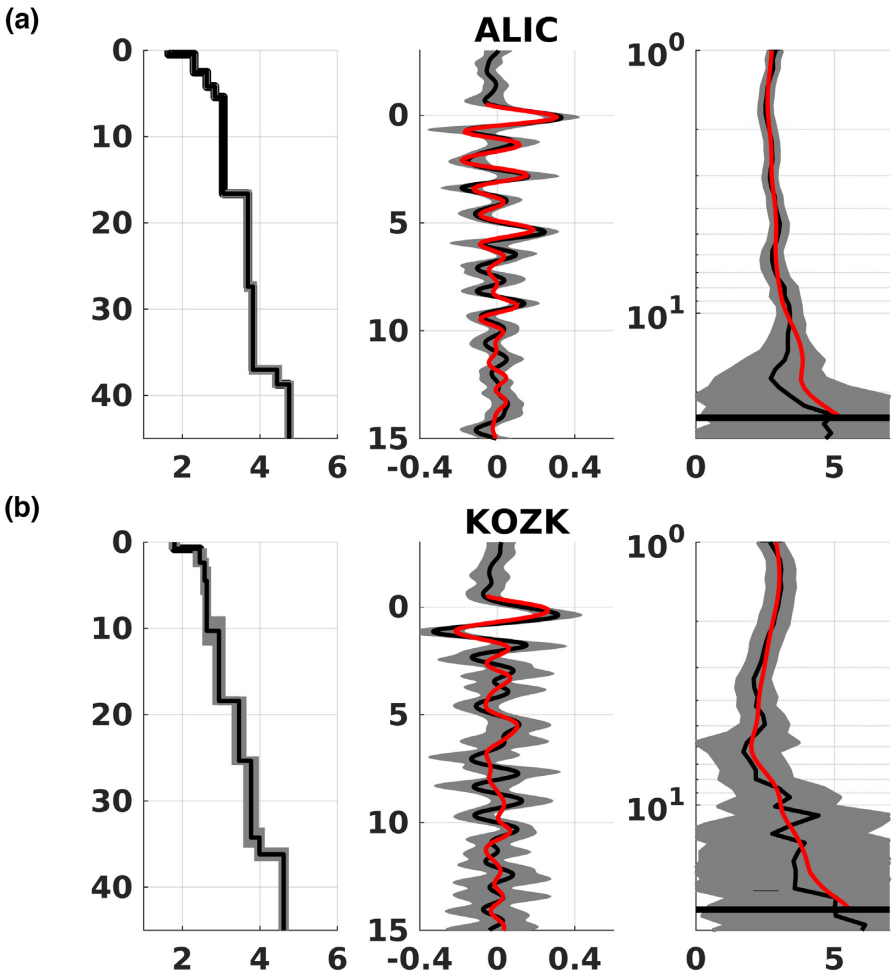

Figure 5. Examples for the final velocity model (left-hand panel), with the corresponding receiver function fit (middle panel) and the Vs_{app} fit (right-hnad panel), for stations ALIC (a) and KOZK (b). Black lines in the middle and right panel show the observed data, red lines represent the best fits, and grey shading are the model error (left-hand panel) and the observed standard deviations of the receiver functions (middle panel) and Vs_{app} (right-hnad panel).

study area (*KIZI, SVSK*), where thinner sedimentary successions coincide with deep crystalline basement. In most other areas, deep basement generally coincides well with thick sedimentary basins, or *vice versa*, though the general character of the depth to basement map appears much smoother than the map of sedimentary thickness (Fig. 8a).

5.3 Moho depth

The Moho is shallow beneath the Çankırı Basin (34–36 km) and deepens abruptly to the north to reach its greatest depth beneath the Central Pontides (40–42 km, Fig. 8c). Locally very shallow Moho is inferred beneath stations *KUZO* and *SEYH* in the central-western part of the study area that straddles the NAFZ. Moderate Moho shallowing is reported at station *SVSK* in the southeast. The Moho is observed at intermediate depths (∼35–38 km) elsewhere across the study area (Fig. 8c). The Moho depth negatively correlates with the sedimentary thickness and depth to basement maps in most areas, that is shallow Moho correlates with thick sedimentary successions and *vice versa*. This relationship is limited by the different wavelength-character of the interfaces (base of sedimentary basins, top of crystalline basement and the Moho). For example, some stations in the Çankırı Basin (CAYA, CORM) and in the east of the study area (BOKE, KUZA, TOKT, KIZI, SVSK, KVT, ARSL) do not show this negative correlation.

5.4 Regional characterization

To further illustrate large-scale variations in geophysical properties across the region, we subdivide the study area into four domains of distinct overall seismic structure, as evaluated from the maps in Figs 6–8. These domains are delimited by major suture zones and are defined as follows (see Fig. 11a): (I) the Istanbul Zone in the northwest, (II) the Eastern Sakarya Zone in the northeast, including the Central and Eastern Pontides (III) the Western Sakarya Zone in the southwest, and (IV) the Çankırı Basin and Kırşehir Massif in the southeast. The seismic properties and structures are averaged for all stations within each of the domains and plotted in Fig. 11(b). A number of interesting patterns emerge from this integrated view. For example, we find that domains I and II show much higher *Vs* values for the upper 5 km (>2.5 km s^{-1}) and 5–15 km depth (>3.2 km s^{-1}) compared to regions III and IV (<2.35 and <3.1 km s^{-1} in the two depth ranges). This is also reflected in the thickness of the sedimentary layer, which is thinnest in domain II (∼1.5 km), followed by domain I (∼2.0 km), compared to an average sedimentary thickness of >2.5 km in domains III and IV. The Moho is deepest in

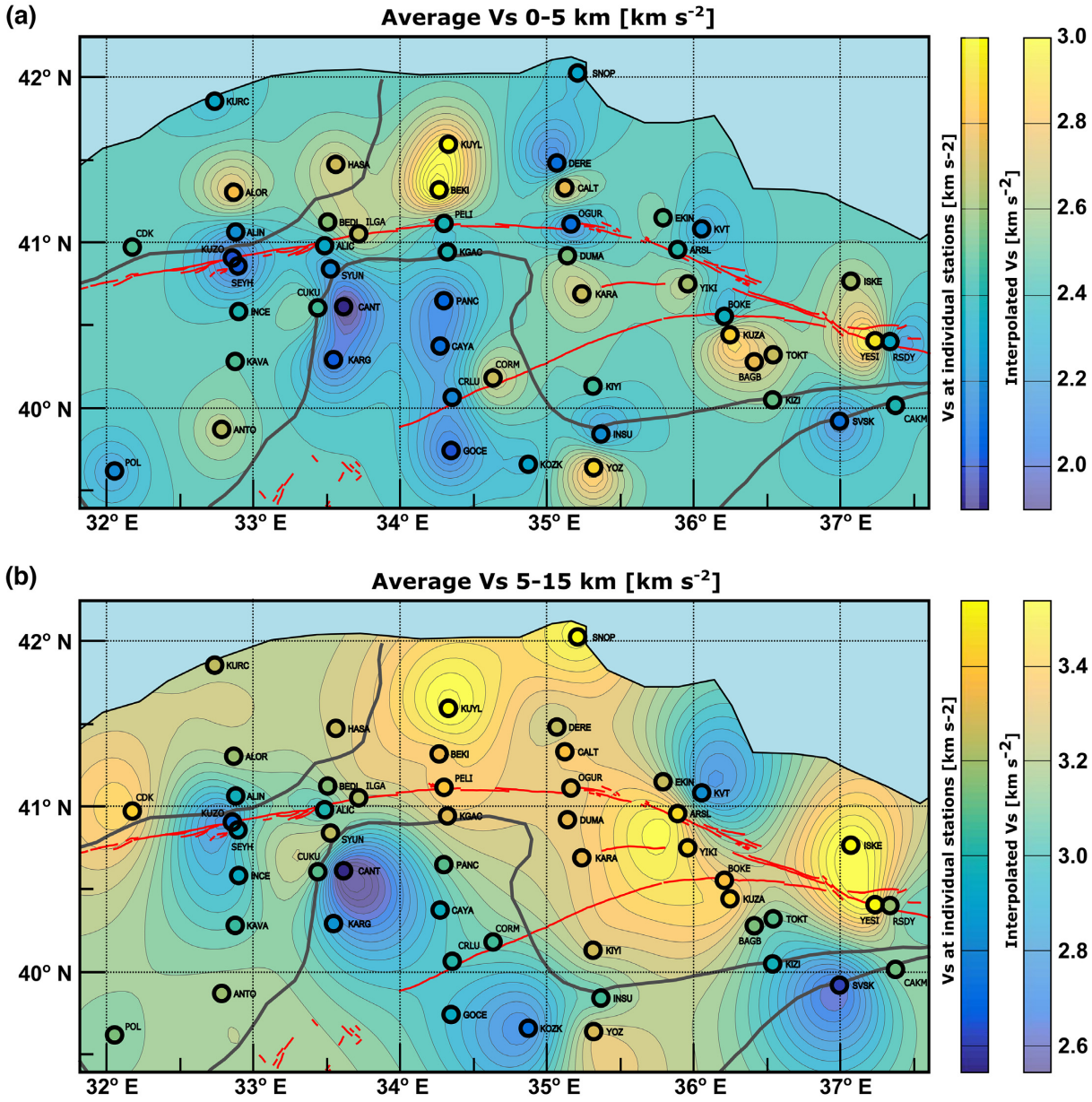

Figure 6. Inversion results in terms of *S*-wave velocities (a) in the upper 5 km of the crust, and (b) in the 5–15 km depth range. The results are shown at individual stations (coloured dots, see left colour bar), and as an interpolated basemap built by kriging the 1-D velocity models obtained at each station (background colours, see right colour bar).

domain II with an average of almost 40 km, intermediate in domain I (∼37.5 km) and thinnest in domains III and IV (∼36 km). Domains II and IV, which together cover the central to eastern portion of our study area, exhibit the most extreme contrast in seismic structure. Domain II has the highest seismic velocities, the thinnest sedimentary layers and the deepest Moho, whereas domain IV is characterized by the lowest velocities, the thickness sedimentary layers and shallowest Moho (together with domain III). These relationships can also be directly assessed by comparing the average RF waveforms from each domain (Fig. 11c). The average RFs from domains I and II show the highest amplitudes for the incident *P* wave ($t = 0$ s), indicative of high uppermost velocities. By contrast, the *P*-wave amplitudes are considerably lower for domains III and IV, indicating low uppermost crustal velocities. This is reflected in the average Vs_{app} curves (Fig. 11d), which are lowest for domain IV, followed by domain III and similarly high for domains I and II. Domains I, III and IV have very similar values of average Vs_{app} at periods $T > 4$ s, while region II clearly has higher velocities at these levels. At $T > 20$ s, velocities lie in a similar range for all domains. The average models and interface interpretations are shown in Fig. 11(e).

6 DISCUSSION

We derived a crustal model of the central NAFZ using a novel inversion of *P*-receiver function and *P*-wave polarization data extracted from teleseismic waveform recorded at 51 broad-band stations. In this section, we discuss our recovered upper-crustal shear-wave velocity structure in light of the tectonic history of the region, known

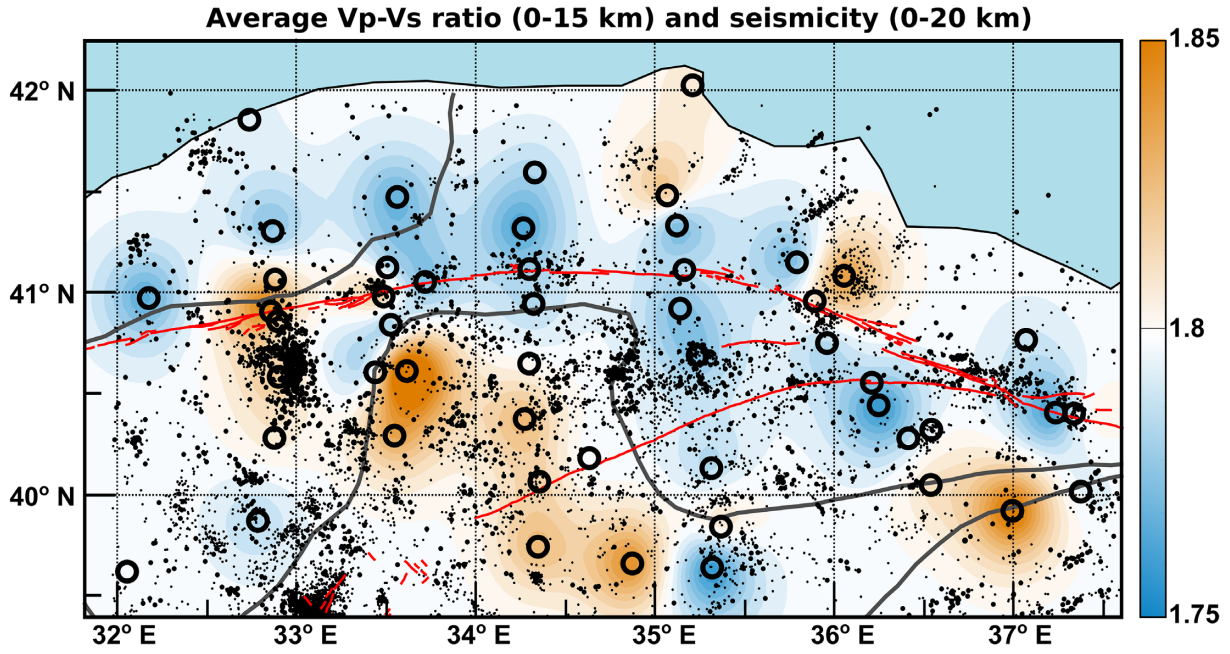

Figure 7. Map of seismicity and *Vp*/*Vs* ratio. Seismicity includes earthquakes with magnitudes greater than 1 (black dots of three sizes: small $M < 3$, medium $M = 3$–4, large $M >= 4$) that occurred between 2005 and 2018 in the upper 20 km of the study area. The basemap is built by kriging *Vp*/*Vs* ratios in the 0–15 km depth range obtained at individual stations. Major faults are denoted by red lines. Sutures are shown as grey lines. Locations, depths and magnitudes of the plotted earthquakes were provided by the Kandilli Observatory and Earthquake Research Institute (see www.koeri.boun.edu.tr). Black circles indicate station locations.

surface expressions of major tectonic boundaries and fault zones, and the distribution of local earthquakes.

6.1 Model uncertainties

Before we discuss the tectonic implications suggested by our inverse modelling, we will describe and discuss the model and data uncertainties. The inversion algorithm uses *a priori* data and model uncertainties (see Section 4). While the data uncertainties are taken directly from the standard deviations of the observed data, the model perturbations are loosely constrained allowing the model to be completely data driven (with exception of the uppermost layer velocity and the lowermost mantle velocity, see Section 4). One output of the inversion is the *a posteriori* covariance matrix consisting of uncertainties for each model parameter from which we derive our model uncertainty estimates (e.g. Tarantola & Valette 1982; Schiffer *et al.* 2015, 2016). The model uncertainties are illustrated in each individual model result as grey shaded areas underlying the velocity models in Fig. 5a and Supplementary File S6. The *a priori* data uncertainties, as well as the three major interpreted discontinuities (sedimentary thickness, depth of basement, Moho depth—converted to delay times) and their *a posteriori* uncertainties, are all shown in Fig. 12 (receiver functions) and 13 (Vs_{app} curves). This provides an overview for all stations of the relative quality of the data and modelling results, and gives a regional context to these quality attributes. Clearly, some stations yield better/more consistent data than others, which is reflected in smaller data uncertainties (grey shaded areas around receiver functions and Vs_{app} curves in Figs 12 and 13). There is no identifiable regional pattern of larger or lower data uncertainties of the receiver functions. Examples of stations with larger receiver function uncertainties include ALIN, ARSL, CANT, ILGA, KOZK, KVT, PANC, POL, SEYH, SVSK. As a result, these stations usually exhibit larger uncertainties in the estimates of the interpreted interfaces and layers (sedimentary basins, depth to basement and Moho, Fig. 12). The large uncertainties in the receiver functions waveforms are also reflected in a wider distribution of the Vs_{app} curves (Fig. 13), but not always. Reciprocally, large uncertainties in Vs_{app} do frequently, but not always, coincide with larger error bars in the receiver functions. Regionally, the Vs_{app} uncertainties seem to show a spatial pattern: stations in areas within sedimentary basins (blue and magenta) generally have larger uncertainties than those stations in areas with very shallow basement (red and cyan).

We also document the uncertainty measures on a set of maps displaying the average errors for *Vs* and layer depths for each station, as well as the RMS data misfit weighted and normalized with the inverse *a priori* data uncertainties (see Supplementary File S7). The latter penalizes the RMS based on data uncertainties, meaning lower RMS when the data uncertainty is high, and *vice versa*. For the models, we find that most *S*-wave velocity errors are of the order of $\sim$0.1–0.15 km s^{-1} and that most depth errors are scattered around a value of 0.5–1 km. The weighted and normalized data misfits show usual values of 0.05–0.2. We do not observe any clear geographical correlation between the distribution high/low model uncertainties and data misfits. Instead, very high/low model uncertainties and data misfits seem to be randomly distributed and do not appear to coincide with one another (Supplementary File S7).

Although our means of estimating uncertainties is formally rooted in the theory of the inverse problem, it appears that these uncertainties are somewhat underestimated. Indeed, the resulting depth and velocity errors appear too low to represent realistic model uncertainties. A common approach to achieve more realistic uncertainties is employing random sampling approaches (e.g. Monte Carlo or Bayesian techniques). However, our inverse algorithm is not currently implemented to apply these approaches, which is why we used the theoretical method described above.

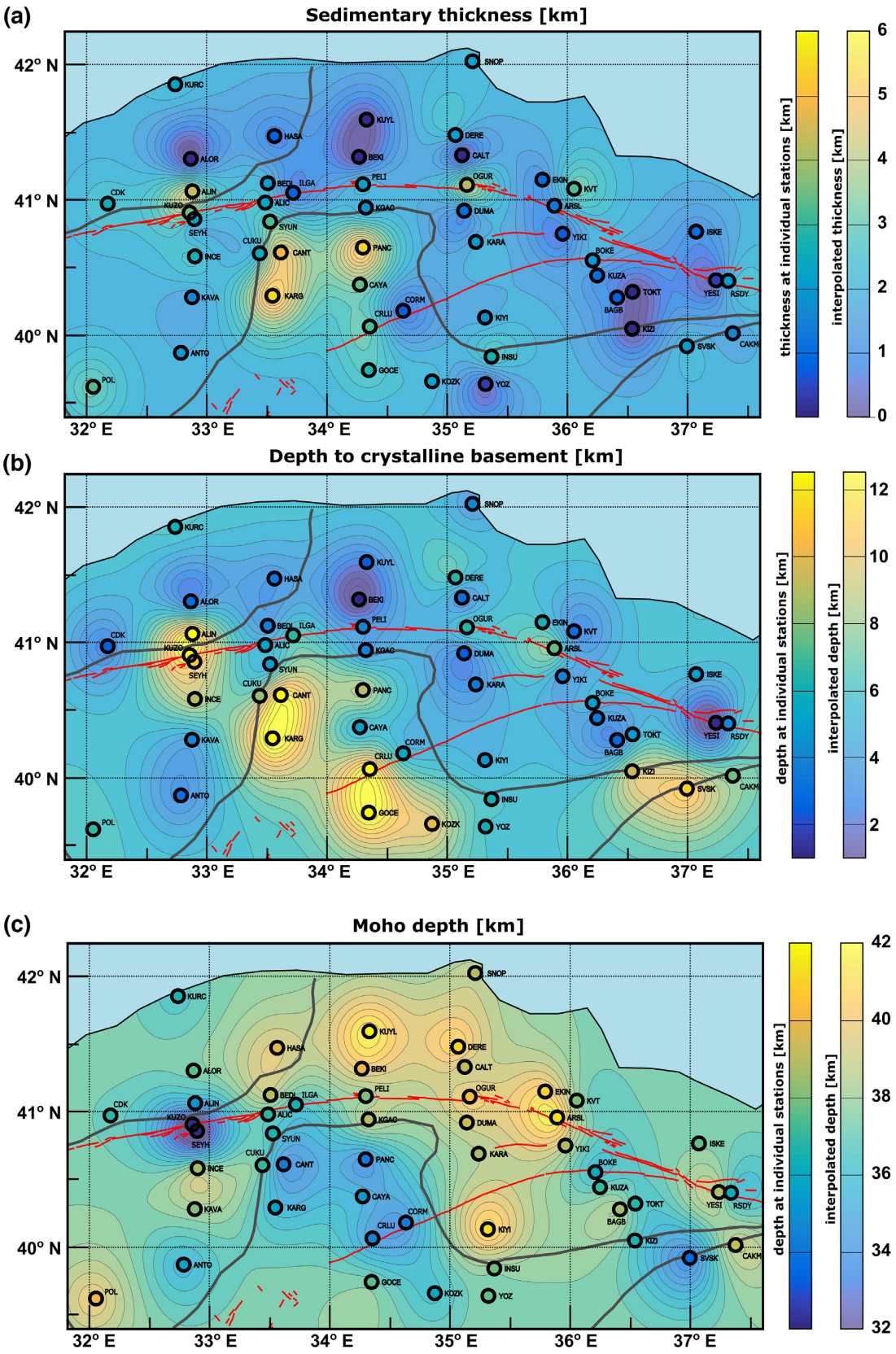

Figure 8. Maps of inferred seismic structures across the study area, in relation to major faults (red lines) and sutures (grey line). (a) Thickness of the uppermost low-velocity sedimentary layer. (b) Depth to crystalline basement (or thickness of sediments and metasediments). (c) Moho depth. The thicknesses/depths are shown at individual stations (coloured dots, see left colour bar), and as an interpolated base map built by kriging the values obtained at each station (background colours, see right colour bar).

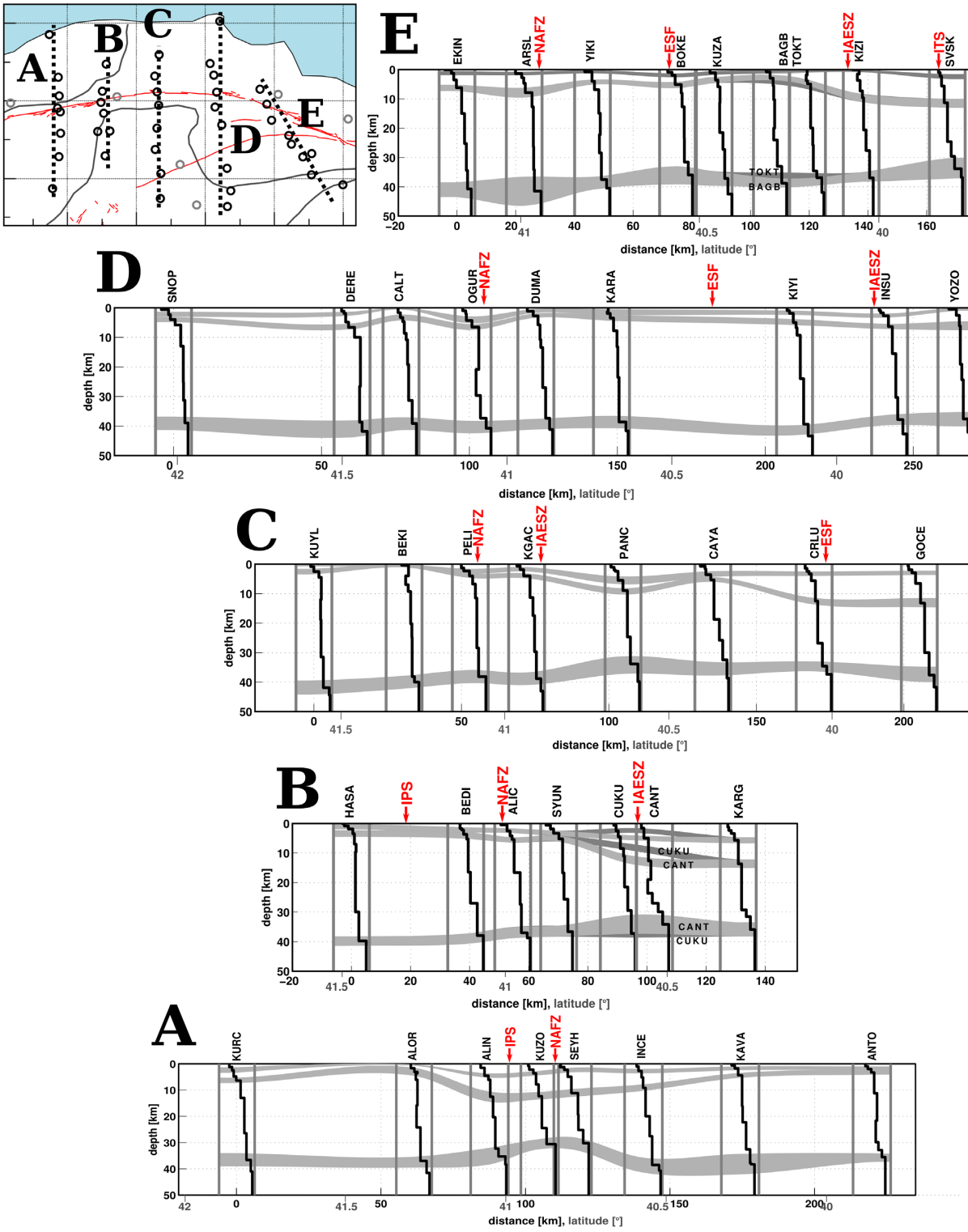

Figure 9. Five N–S profiles through the study area showing the 1-D *S*-wave velocity profiles from joint inversion. Inset shows the outline of the study area, as well as the locations of the five profiles (A–E) and the seismic stations (black circles are stations used and grey circles are stations not used in the profiles). The approximate location of the North Anatolian Fault Zone (NAFZ), the Intra Pontide Suture (IPS), the Izmir-Ankara-Erzincan Suture Zone (IAESZ) and the Ezinepazari-Sungurlu Fault (ESF) are marked in the profiles. The grey bands in the background represent the three main interpreted interfaces, including the model error. These interfaces are, from top to bottom: base of the uppermost low-velocity sedimentary layer, base of the crystalline basement, and the Moho. Note that, in two instances, pairs of very closely spaced stations were used for the interpretation. In this case, we spatially separated the station from another and also separated the interpretation from each station for visualization purposes: CUKU and TOKT are in dark grey, whereas CANT and BAGB are in light grey. The velocity profiles are plotted in individual grey boxes for each station along the profile, with vertical grey lines marking *S*-wave velocities of 1 and 4.8 km s^{-1}.

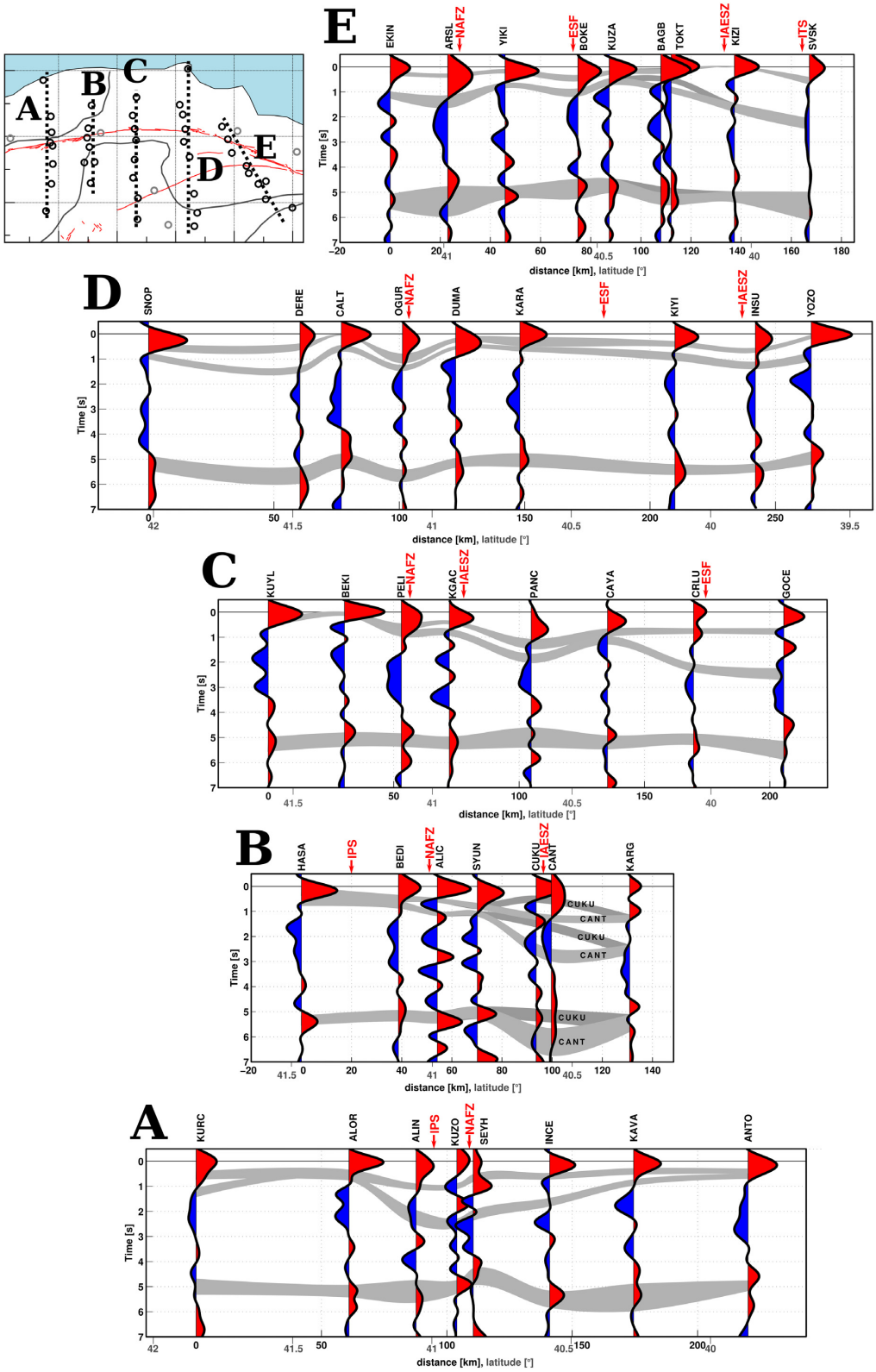

Figure 10. Same N–S profiles as for Fig. 9 showing the receiver function waveforms, along with the interpreted interfaces and their error bars in the delay-time domain. For details see caption of Fig. 9. At most stations, the interfaces correspond to clear signals in the receiver function waveform. However, there are a few cases where a clear signal is missing, which can be explained by a combination of generally weaker Moho discontinuities (gradients or the presence of high velocity lower crust) and the interference with sedimentary or intracrustal multiples. Consistent with this explanation, weak Moho signals tend to be associated with a large sedimentary thickness (e.g. stations CUKU, CANT, PANC, OGUR, KIZI, SVSK). It should be noted that the receiver function delay time shown in this figure are depended on but neither equivalent nor proportional to depth. For example, the large Moho delay time at station CANT, in profile B, is due to a very thick sedimentary basin rather than large Moho depth.

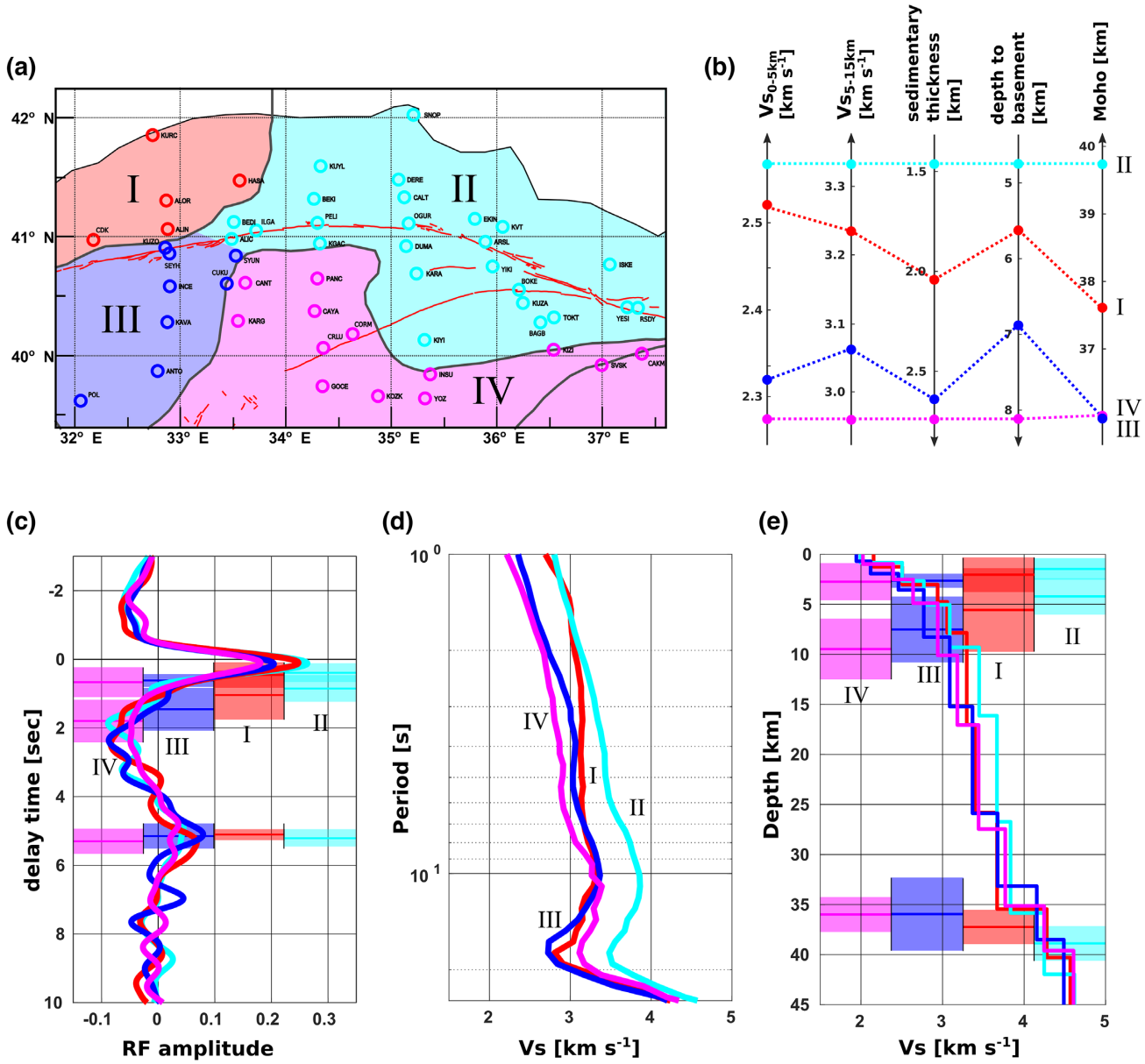

Figure 11. Summary of inversion results for the study area. (a) The study area is divided into four domains (I—red, II—light blue, III—dark blue, and IV—magenta). (b) Mean values of seismic properties and structures for each domain: *S*-wave velocity in the upper 5 km, the *S*-wave velocity in the 5–15 km depth range, inferred sedimentary thickness, inferred depth to basement and inferred Moho depth. It is apparent that domain IV exhibits the lowest velocities, shallowest Moho and deepest basins. It is followed by domain III, whereas the northern portion of the study area (domains I–II) exhibit generally high uppermost velocities, shallow basins and deep Moho. (c) Receiver function stacks for each domain. Note the clearly lower *P*-wave amplitudes for domains III–IV, compared to domains I–II, indicating low uppermost velocities in the south of the study area. Horizontal bars mark the average estimate of the sedimentary thickness, depth to basement and depth to Moho (converted to delay time) and shaded areas mark the respective variation in each region. (d) Mean Vs_{app} curves for each domain. Domains III–IV show lower uppermost *S*-wave velocities compared to domains I–II. (e) *S*-wave velocity-depth profiles for each region, in which every of the eight model layers is averaged. Horizontal bars mark the average estimate of the sedimentary thickness, depth to basement and depth to Moho and shaded areas mark the respective variation in each region.

6.2 The depth extent of the NAFZ

Localized shear deformation along the continental strike-slip fault system of the NAFZ is regarded as the primary source of seismic hazard in the region. Local earthquake clusters have been detected along various segments of the NAFZ, with seismicity generally focussed in the upper 15 km of the crust (Taymaz *et al.* 2001; Bulut *et al.* 2009; Poyraz *et al.* 2015; Bohnhoff *et al.* 2016). Accurate earthquake locations and earthquake cluster geometries are crucial information for understanding strain accumulation during the earthquake cycle and the assessment of seismic hazard, but are not well resolved at mid- to lower-crustal depths. Hence, a highly debated question is how far strike-slip deformation extends at depth.

Our results from the central NAFZ indicate a strong correlation of the entire crustal velocity structure with surface expressions of faults and terrane boundaries. The NAFZ appears to form a boundary between two regions of differing crustal characteristics, based on both crustal velocity distributions (Fig. 6) and interpreted Moho

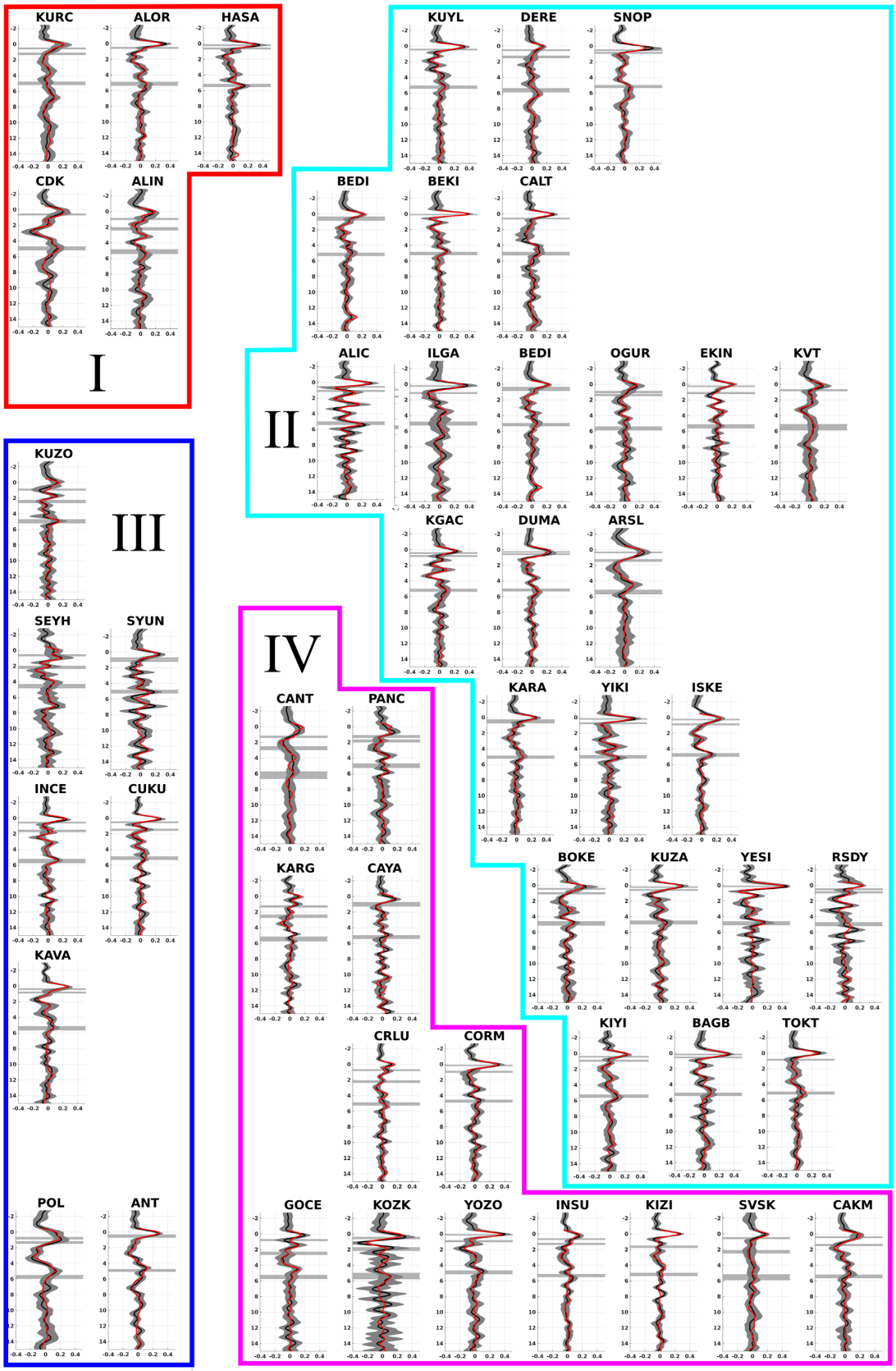

Figure 12. Receiver function stacks of all stations arranged in their approximate station geometry and sorted in their respective region (red—region I, cyan—region II, blue—region III, magenta—region IV). Black lines show the observed data, red lines represent the best fits, and grey shading are the observed standard deviations of the receiver functions. Grey shaded horizontal bars represent the estimates of sedimentary thickness, depth to basement and Moho depth converted to delay time—the thickness of the bar represents the mathematical error on these interfaces from the inversion. Each individual axis is identical to the axes in Fig. 5 (middle panels).

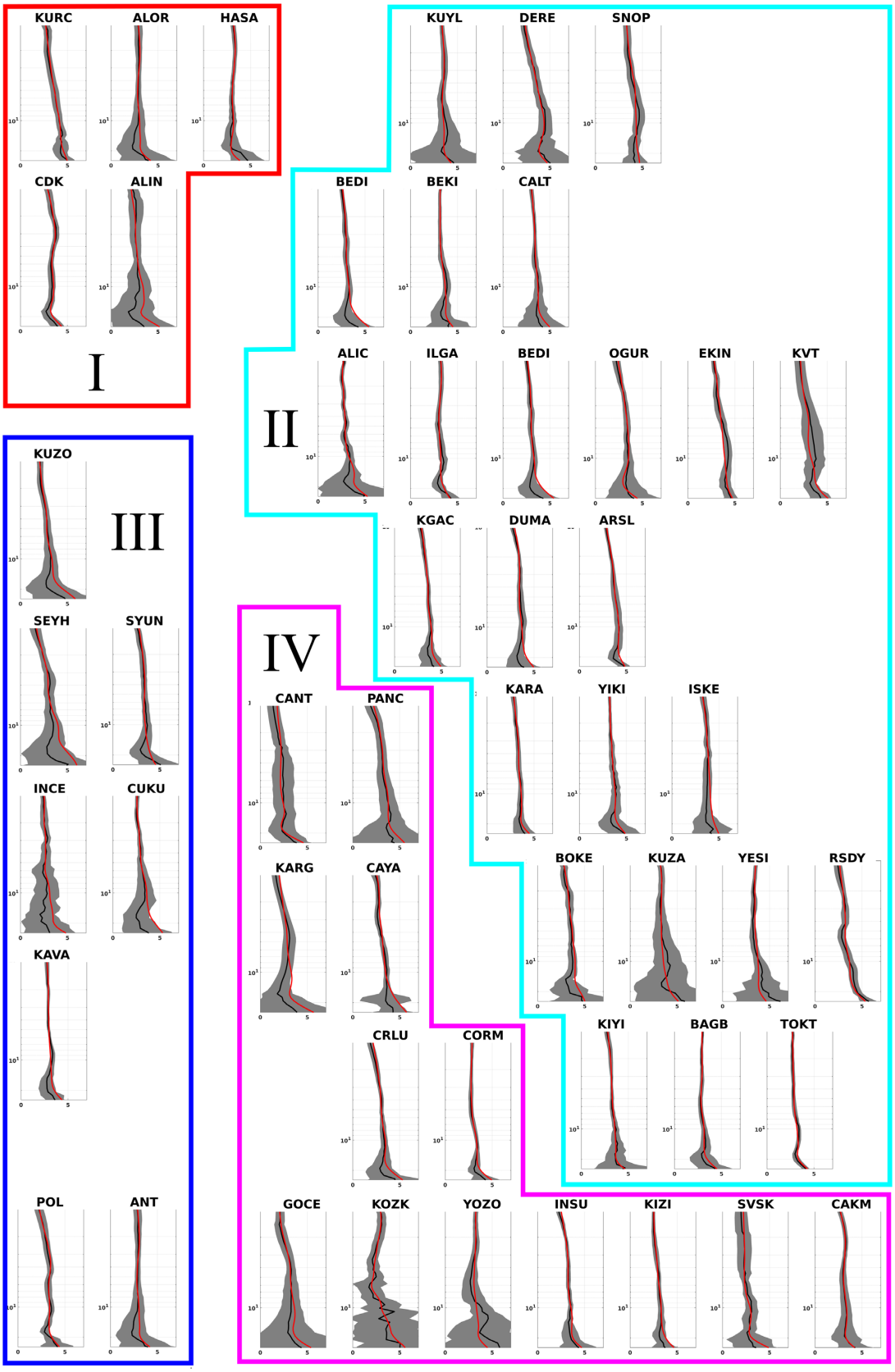

Figure 13. Vs_{app} curves of all stations arranged in their approximate station geometry and sorted in their respective region (red—region I, cyan—region II, blue—region III, magenta—region IV). Black lines show the observed data, red lines represent the best fits, and grey shading are the observed standard deviations of the Vs_{app}. Each individual axis is identical to the axes in Fig. 5 (right-hand panel).

depth (Figs 8 and 9): (1) a northern region where crustal attributes vary over large wavelengths, with thick crust under the Central Pontides and intermediate crust elsewhere; (2) a southern region where crustal attributes vary over shorter wavelengths, with small-scale basins and basement highs. These observations are better explained by focused deformation in the crust (more rigid behaviour), rather than by a broader depth-distributed deformation pattern (more ductile behaviour). In their recent *S*-wave tomography, Papaleo *et al.* (2018) have also reported focused deformation for a northwestern segment of the NAFZ, with a width of ∼10 km at upper crustal depths that widens to ∼30 km at lower crustal depths. Focussed deformation in the upper crust is also consistent with the strong radial anisotropy ($V_{SV} > V_{SH}$) that has been measured close to the NAFZ down to 20–25 km depth (Çubuk-Sabuncu *et al.* 2017). Such seismic anisotropy may develop from reorientation of rock fabrics during deformation, especially along strike slip faults (Storti *et al.* 2003). Similarly, local shear wave splitting and converted wave analyses along the western and central part of the NAFZ imply strong anisotropy related to major faults at depths of down to 15–20 km, often asymmetrically distributed with regards on both sides of the fault (e.g. Peng & Ben-Zion 2004; Hurd & Bohnhoff 2012; Eken *et al.* 2013a; Liccardi *et al.* 2018).

Looking deeper into the lithosphere under the NAFZ, some tomographic results based on inversion of teleseismic *P* waves (Biryol *et al.* 2011) and full waveforms (Fichtner *et al.* 2013a,b) indicate a sharp velocity contrast across the NAFZ reaching down to 100–150 km depth. In contrast, results from Rayleigh wave tomography could not detect any significant velocity changes across the NAFZ within the mantle lithosphere (Salaün *et al.* 2012). A comprehensive shear-wave splitting study across the region indicates that there is a systematic obliquity between the crustal and mantle anisotropy beneath the NAFZ (Paul *et al.* 2014), further suggesting that NAFZ deformation is limited to the crust and decoupled from the mantle. This behaviour is different from observations in northeast Tibet, where fast anisotropy directions are nearly parallel to the strike of the North and South Kunlun faults, indicating a vertically coherent deformation transmitted within the entire lithosphere (León Soto *et al.* 2012; Eken *et al.* 2013b).

In summary, we find that deformation along the central NAFZ appears to be focussed in the crust, which is consistent with a number of previous studies. However, seismic observations of the lithospheric mantle are inconsistent with regards to how (or if) NAFZ deformation extends to greater depths. Hence, the issue of how strike-slip deformation is manifested in the mantle remains unresolved.

6.3 Lithological contrasts

Şengör *et al.* (2005) have previously discussed a possible asymmetric distribution of elastic properties across the NAFZ by identifying lithological contrasts produced by lateral displacement along the NAFZ. Such lithological contrasts have been previously imaged across the region by 3-D seismic tomography (e.g. Yolsal-Çevikbilen *et al.* 2012; Fichtner *et al.* 2013a, b; Delph *et al.* 2015; Çubuk-Sabuncu *et al.* 2017), fault-guided head wave analyses (Bulut *et al.* 2012; Najdahmadi *et al.* 2016) and 2-D/3-D geoelectric methods (Kaya *et al.* 2013). Our results show that the fault zones (most notably the NAFZ) seem to accommodate rough, small-wavelength velocity perturbations indicative of small basins and basement highs distributed in the vicinity of the fault line. These small-wavelength variations extend down to the Moho but appear to be concentrated at basin and basement depths. The character of the velocity structure appears to become smoother away from the faults. In contrast, we observe that the suture zones crossing the study area strongly correlate with larger-scale velocity variations and crustal structure inferred from the maps in Figs 6–8 and the profiles in Fig. 9. In particular, the IAESZ provides a clear outline to the velocity structures marking the Çankırı Basin. Suture zones between different accreted terranes often mark boundaries between different lithologies and compositions and this is clearly illuminated by our seismic inversion. Subdividing the study area into several zones based on similar seismic and crustal characteristics, as we have done in Section 5.4, reflects the strong segmentation of the study area by the major tectonic boundaries and implies a dominant control of the tectonic history on crustal structure (Fig. 11).

6.4 Sedimentary infill

At regional scale, infill of sediments (both old and young) is most prominent and continuous across the Çankırı Basin and parts of the Kırşehir Massif. Sedimentary and metasedimentary layers have large thicknesses in the Çankırı Basin. The basement is deep in the southern and eastern Kırşehir Massif, but only thin uppermost sediments are observed there, indicating a thick metasedimentary succession.

At local scale, one would expect deformation and lateral offsets associated with major transform fault systems to produce complex localized structures along the fault zones, including small sedimentary basins. Our sedimentary thickness and depth to basement maps do indeed show small-scale variations concentrated along the NAFZ, suggesting the existence of such structures (small basins and basement highs) that are likely caused by deformation proximal to the NAFZ.

A set of stations (*KUZO, SEYH*, and to some degree *ALIN, INCE*), which are located close to the NAFZ at approximately 41° N, 33° W, exhibit large apparent sedimentary thicknesses (*ALIN, KUZO*), deep basement (*KUZO, SEYH*, *ALIN, INCE*) and shallow Moho (*KUZO, SEYH*). Though these observations may stem from real localized geological features, we must also consider the possibility that they are artefacts caused by strong seismic anisotropy (see, e.g. Licciardi *et al.* 2018) and/or complex scattering patterns from fractured/deformed rocks or localized geological bodies along the NAFZ that act as point scatterers. A recent inversion of coda wave envelopes in the same study area indicates that the effect of scattering attenuation should be relatively small compared to the intrinsic attenuation (Gaebler *et al.* under review). Thus, we can exclude scattering from the potential sources of artefacts. Further work beyond the scope of this paper will be required to assess these effects.

6.5 Crustal strength and seismicity along the fault

An open question is how seismicity is distributed along fault zones. The NAFZ is related to elevated seismic activity, which has included a number of damaging earthquakes (Taymaz *et al.* 1991, 2001; Bohnhoff *et al.* 2016), but the factors that control the location and mechanism of these earthquakes are not well understood. The occurrence of earthquakes maybe related to a complex interplay between plate motions, the shape of the fault zone/plate boundary and rheological variations in the lithosphere (Chester *et al.* 1993; Lyakhovsky *et al.* 2001). To see whether our results can help address these questions, we propose to investigate the *Vp*/*Vs* ratio of the upper 15 km of the crustal model (i.e. a measure of crustal

weakness in the mostly brittle part of the crust) in conjunction with the seismicity in the upper 20 km recorded since 2005 (Fig. 7).

Although it is difficult to establish any robust correlation from the map in Fig. 7, earthquakes appear to cluster along the active faults and around regions of high *Vp*/*Vs* ratios (or possibly at high *Vp*/*Vs* ratio gradients). Such high *Vp*/*Vs* ratios, if caused by high pore pressures and/or water-filled microcracks (Gudmundsson 1999; Zhao 2015), could be associated with weak zones that may accommodate deformation and seismic activity. Moreover, lateral variations of high and low *Vp*/*Vs* ratio in the study area correlate well with the distribution of harmonic energy values marking regions of strong anisotropy (Liccardi *et al.* 2018), which may be linked to extensive dilatancy of fluid-filled microcracks within the top 15 km of the crust. Our results suggest that, at least to some degree, the boundaries between weak and strong upper crustal domains or the edges of weak zones (white areas in Fig. 7) may focus deformation. We note however that large parts of the study area lack sufficient station coverage to map crustal properties well enough to draw additional conclusions. New seismic deployments are thus needed to further test the hypothesized link between crustal boundaries and focused deformation. The southwestern portion of the study area, which hosts a large earthquake cluster centred at ∼39.5°N, ∼33°E, is a particularly attractive target for future deployments. Other potential targets include earthquake clusters at ∼40.5°N, ∼33°E and at ∼40.5°N, ∼35°E.

7 CONCLUSION

Our novel joint inversion of *P*-receiver functions and *P*-wave polarization provides estimates of crustal velocity structure in the central NAFZ. We identify considerable velocity variations (Vs = 1.9–3.55 km s^{-1}) at upper crustal levels that correspond to known tectonic structures and lineaments in the study area. Velocities in the uppermost 5 km outline the boundaries between sedimentary basins (low velocities) and basement highs (high velocities). The most prominent feature in this depth range is the Çankırı Basin, which is clearly outlined by the IAESZ. Smaller basins are also inferred in vicinity to the NAFZ. Velocity contrasts in the 5–15 km depth range mainly correspond to different crustal blocks. The IAESZ still appears as a major boundary at these depths, separating areas of different crustal velocities. In particular, the Çankırı Basin and the Kırşehir Massif are still well-visible. The NAFZ also seems to act as a large-scale boundary between crustal blocks of differing elastic properties to the north and south of the fault zone. These observations are reflected in our maps of crustal attributes (sedimentary thickness, depth to basement, Moho depth) across the region. Our maps reveal that these crustal attributes exhibit a rougher character (i.e. small-scale highs and lows) along the NAFZ compared to regions away from the fault zone. Such small-scale variations are likely due to localized deformation concentrated in the proximity of the NAFZ. The maps reinforce the notion that the NAFZ represents a fundamental boundary in crustal properties between north and south, with a sharp lateral contrast extending down to Moho depth. To the south of the NAFZ, Moho depths variations occur over small scales, with several areas exhibiting local highs and lows. In contrast, to the north, a single thick crustal block is observed in the central part with intermediate Moho depth to the west and east. These results suggest that the NAFZ is a feature that extends through the entire crustal column with relatively narrow/localized deformation. Seismicity appears to cluster around areas of low *Vp*/*Vs* ratios, which are interpreted as potential weak zones. Our results complement a wealth of previous geophysical, geodetic and geological analyses that have been carried out across the NAFZ. Taken together, all these results provide new insight into the relationships between crustal structure, tectonic boundaries and seismicity. They help in expanding a vital geoscientific discussion whose ultimate goal is the understanding of deformation, seismicity and associated seismic hazard in the region.

ACKNOWLEDGEMENTS

We want to thank two anonymous reviewers for constructive comments and the editors for handling the paper. This work was conducted during Christian Schiffer's postdoctoral research fellowship at Durham University funded by the Carlsberg Foundation (Denmark) and within the framework of a project (ITU-BAP 39031) that is financially supported by Istanbul Technical University, Scientific Research Program (ITU-BAP). We are grateful to the Incorporated Research Institutions for Seismology Data Management Center (IRIS-DMC) and the ORFEUS Data Center for making continuous broad-band data open to the international scientific community. Data for the NAF experiment (doi: https://doi.org/10.7914/SN/YL_2005) are available from the IRIS Data Management Center at http://www.iris.edu/hq/. Tuna Eken and Tuncay Taymaz acknowledge financial support from Alexander von Humboldt Foundation (AvH) towards computational and peripherals resources. Stéphane Rondenay's contribution to this work was supported by Career Integration Grant 321871- GLImER from the FP7 Marie Curie Actions of the European Commission and by the Research Council of Norway FRINATEK programme through SWaMMIS project 231354

REFERENCES

Amante, C. & Eakins, B.W., 2009. ETOPO1 1 arc-minute global relief model: procedures, data sources and analysis, NOAA Tech. Memo. NESDIS NGDC-24, National Geophysical Data Center, NOAA, doi:10.7289/V5C8276M.

Ammon, C.J., 1991. The isolation of receiver effects from teleseismic P waveforms, *Bull. seism. Soc. Am.,* **81,** 2504–2510.

Ammon, C.J., Randall, G.E. & Zandt, G., 1990. On the nonuniqueness of receiver function inversions, *J. geophys. Res.: Solid Earth,* **95,** 15 303–15 318.

Barka, A.A., 1992. The north Anatolian fault zone, *Ann. Tectonicae,* **6,** 164–195.

Bayrakci, G., Laigle, M., Bécel, A., Hirn, A., Taymaz, T., Yolsal-Çevikbilen, S. & Team, S., 2013. 3-D sediment-basement tomography of the Northern Marmara trough by a dense OBS network at the nodes of a grid of controlled source profiles along the North Anatolian fault, *Geophys. J. Int.,* **194,** 1335–1357.

Biryol, C.B., Beck, S.L., Zandt, G. & Özacar, A.A., 2011. Segmented African lithosphere beneath the Anatolian region inferred from teleseismic P-wave tomography, *Geophys. J. Int.,* **184,** 1037–1057.

Biryol, C.B., Zandt, G., Beck, S.L., Ozacar, A.A., Adiyaman, H.E. & Gans, C.R., 2010. Shear wave splitting along a nascent plate boundary: the North Anatolian Fault Zone, *Geophys. J. Int.,* **181,** 1201–1213.

Bohnhoff, M., Martínez-Garzón, P., Bulut, F., Stierle, E. & Ben-Zion, Y., 2016. Maximum earthquake magnitudes along different sections of the North Anatolian fault zone, *Tectonophysics,* **674,** 147–165.

Bulut, F., Bohnhoff, M., Eken, T., Janssen, C., Kılıç, T. & Dresen, G., 2012. The East Anatolian Fault Zone: Seismotectonic setting and spatiotemporal characteristics of seismicity based on precise earthquake locations, *J. geophys. Res.: Solid Earth,* **117,** B07304, doi:10.1029/2011JB008966.

Bulut, F., Bohnhoff, M., Ellsworth, W.L., Aktar, M. & Dresen, G., 2009. Microseismicity at the North Anatolian fault in the Sea of Marmara offshore Istanbul, NW Turkey, *J. geophys. Res.: Solid Earth,* **114,** .

Bürgmann, R. & Dresen, G., 2008. Rheology of the lower crust and upper mantle: evidence from rock mechanics, geodesy, and field observations, *Annu. Rev. Earth planet. Sci.,* **36,** 531–567.

Cassidy, J.F. & Ellis, R.M., 1993. S wave velocity structure of the northern cascadia subduction zone, *J. geophys. Res.: Solid Earth,* **98,** 4407–4421.

Chester, F.M., Evans, J.P. & Biegel, R.L., 1993. Internal structure and weakening mechanisms of the San Andreas fault, *J. geophys. Res.: Solid Earth,* **98,** 771–786.

Chong, J., Chu, R., Ni, S., Meng, Q. & Guo, A., 2018. Receiver function HV ratio: a new measurement for reducing non-uniqueness of receiver function waveform inversion, *Geophys. J. Int.,* **212,** 1475–1485.

Christensen, N.I., 1996. Poisson's ratio and crustal seismology, *J. geophys. Res.: Solid Earth,* **101,** 3139–3156.

Christensen, N.I. & Mooney, W.D., 1995. Seismic velocity structure and composition of the continental crust: a global view, *J. geophys. Res.: Solid Earth,* **100,** 9761–9788.

Clayton, R.W. & Wiggins, R.A., 1976. Source shape estimation and deconvolution of teleseismic bodywaves, *Geophys. J. R. astr. Soc.,* **47,** 151–177.

Çubuk-Sabuncu, Y., Taymaz, T. & Fichtner, A., 2017. 3-D crustal velocity structure of western Turkey: constraints from full-waveform tomography, , *Phys. Earth planet. Inter.,* **270,** 90–112.

Çubuk-Sabuncu, Y., Yolsal-Çevikbilen, S. & Taymaz, T., 2014. Source parameters of Bala-Sirapinar (Central Turkey) Earthquakes of 2005–2008: Implications on internal deformations of the anatolian plate, *Tectonophysics,* **635,** 125–153.

Darbyshire, F.A., 2003. Crustal structure across the Canadian High Arctic region from teleseismic receiver function analysis, *Geophys. J. Int.,* **152,** 372–391.

Delph, J.R., Biryol, C.B., Beck, S.L., Zandt, G. & Ward, K.M., 2015. Shear wave velocity structure of the Anatolian Plate: anomalously slow crust in southwestern Turkey, *Geophys. J. Int.,* **202,** 261–276.

Dewey, J. & Şengör, A.M.C., 1979. Aegean and surrounding regions: complex multiplate and continuum tectonics in a convergent zone, *GSA Bull.,* **90,** 84–92.

Eken, T., Bohnhoff, M., Bulut, F., Can, B. & Aktar, M., 2013a. Crustal anisotropy in the eastern sea of marmara region in Northwestern Turkey crustal anisotropy in the Eastern Sea of marmara region in Northwestern Turkey, *Bull. seism. Soc. Am.,* **103,** 911–924.

Eken, T., Tilmann, F., Mechie, J., Zhao, W., Kind, R., Su, H., Xue, G. & Karplus, M., 2013b. Seismic anisotropy from SKS Splitting beneath Northeastern TibetShort Note, *Bull. seism. Soc. Am.,* **103,** 3362–3371.

Fichtner, A., Saygin, E., Taymaz, T., Cupillard, P., Capdeville, Y. & Trampert, J., 2013a. The deep structure of the North Anatolian Fault Zone, *Earth planet. Sci. Lett.,* **373,** 109–117.

Fichtner, A., Trampert, J., Cupillard, P., Saygin, E., Taymaz, T., Capdeville, Y. & Villaseñor, A., 2013b. Multiscale full waveform inversion, *Geophys. J. Int.,* **194,** 534–556.

Fouch, M.J. & Rondenay, S., 2006. Seismic anisotropy beneath stable continental interiors, *Phys. Earth planet. Inter.,* **158,** 292–320.

Gaebler, P., Eken, T., Bektaş, H.Ö., Wegler, U. & Taymaz, T., under review. Shear wave attenuation along the central part of the North Anatolian fault zone, *J. Seismol.*

Gans, C.R., Beck, S.L., Zandt, G., Biryol, C.B. & Ozacar, A.A., 2009. Detecting the limit of slab break-off in central Turkey: new high-resolution Pn tomography results, *Geophys. J. Int.,* **179,** 1566–1572.

Gudmundsson, A., 1999. Fluid overpressure and stress drop in fault zones, *Geophys. Res. Lett.,* **26,** 115–118.

Hannemann, K., Krüger, F., Dahm, T. & Lange, D., 2016. Oceanic lithospheric S-wave velocities from the analysis of P-wave polarization at the ocean floor, *Geophys. J. Int.,* **207,** 1796–1817.

Hurd, O. & Bohnhoff, M., 2012. Stress-and structure-induced shear-wave anisotropy along the 1999 Izmit Rupture, Northwest Turkey, *Bull. seism. Soc. Am.,* **102,** 2177–2188.

Jacobsen, B.H. & Svenningsen, L., 2008. Enhanced uniqueness and linearity of receiver function inversion, *Bull. seism. Soc. Am.,* **98,** 1756–1767.

Kahraman, M. *et al.*, 2015. Crustal-scale shear zones and heterogeneous structure beneath the North Anatolian Fault Zone, Turkey, revealed by a high-density seismometer array, *Earth planet. Sci. Lett.,* **430,** 129–139.

Karabulut, H., Özalaybey, S., Taymaz, T., Aktar, M., Selvi, O. & Kocaoğlu, A., 2003. A tomographic image of the shallow crustal structure in the Eastern Marmara, *Geophys. Res. Lett.,* **30,** 2277.

Karasözen, E., Özacar, A.A., Biryol, C.B. & Beck, S.L., 2013. Seismicity, focal mechanisms and active stress field around the central segment of the North Anatolian Fault in Turkey, *Geophys. J. Int.,* **196,** 405–421.

Kaya, T., Kasaya, T., Tank, S.B., Ogawa, Y., Tunçer, M.K., Oshiman, N., Honkura, Y. & Matsushima, M., 2013. Electrical characterization of the North Anatolian Fault Zone underneath the Marmara Sea, Turkey by ocean bottom magnetotellurics, *Geophys. J. Int.,* **193,** 664–677.

Kaymakçı, N., 2000. *Tectono-Stratigraphical Evolution of the Çankırı Basin (Central Anatolia, Turkey),* Utrecht University.

Kaymakçı, N., White, S.H. & Vandijk, P.M., 2003. Kinematic and structural development of the Çankiri Basin (Central Anatolia, Turkey): a paleostress inversion study, *Tectonophysics,* **364,** 85–113.

Kaymakçı, N., Özçelik, Y., White, S.H. & Van Dijk, P.M., 2009. Tectonostratigraphy of the Çankırı Basin: late Cretaceous to early Miocene evolution of the Neotethyan suture zone in Turkey, *Geol. Soc. Lond. Spec. Publ.,* **311,** 67–106.

Koulakov, I., Bindi, D., Parolai, S., Grosser, H. & Milkereit, C., 2010. Distribution of seismic velocities and attenuation in the crust beneath the North Anatolian Fault (Turkey) from Local Earthquake Tomography, , *Bull. seism. Soc. Am.,* **100,** 207–224.

Langston, C.A., 1979. Structure under Mount Rainier, Washington, inferred from teleseismic body waves, *J. geophys. Res.: Solid Earth,* **84,** 4749–4762.

Le Pichon, X., Şengör, A.M.C., Kende, J., İmren, C., Henry, P., Grall, C. & Karabulut, H., 2015. Propagation of a strike-slip plate boundary within an extensional environment: the westward propagation of the North Anatolian Fault, *Can. J. Earth Sci.,* **53,** 1416–1439.

León Soto, G., Sandvol, E., Ni, J.F., Flesch, L., Hearn, T.M., Tilmann, F., Chen, J. & Brown, L.D., 2012. Significant and vertically coherent seismic anisotropy beneath eastern Tibet, *J. geophys. Res.: Solid Earth,* **117,** B05308, doi:10.1029/2011JB008919.

Liccardi, A., Eken, T., Agostnetti, N.P., Yolsal-Çevikbilen, S., Tilmann, F. & Taymaz, T., 2018. Seismic anisotropy in central North Anatolian Fault Zone and its implications on crustal deformation, *Phys. Earth planet. Inter.,* **277,** 99–112.

Lophaven, S.N., Nielsen, H.B. & Søndergaard, J., 2002. DACE-A Matlab Kriging toolbox, version 2.0.

Lyakhovsky, V., Ben-Zion, Y. & Agnon, A., 2001. Earthquake cycle, fault zones, and seismicity patterns in a rheologically layered lithosphere, *J. geophys. Res.: Solid Earth,* **106,** 4103–4120.

Menke, W., 1989. *Geophysical Data Analysis: Discrete Inverse Theory,* Academic Press.

Molnar, P. & Dayem, K.E., 2010. Major intracontinental strike-slip faults and contrasts in lithospheric strength, *Geosphere,* **6,** 444–467.

Najdahmadi, B., Bohnhoff, M. & Ben-Zion, Y., 2016. Bimaterial interfaces at the Karadere segment of the North Anatolian Fault, northwestern Turkey, *J. geophys. Res.: Solid Earth,* **121,** 931–950.

Nakamura, A. *et al.*, 2002. P-wave velocity structure of the crust and its relationship to the occurrence of the 1999 İzmit, Turkey, earthquake and aftershocks, *Bull. seism. Soc. Am.,* **92,** 330–338.

Ottemöller, L. & Midzi, V., 2003. The crustal structure of Norway from inversion of teleseismic receiver functions, *J. Seismol.,* **7,** 35–48.

Owens, T.J., Taylor, S.R. & Zandt, G., 1987. Crustal structure at regional seismic test network stations determined from inversion of broadband teleseismic P waveforms, *Bull. seism. Soc. Am.,* **77,** 631–662.

Papaleo, E., Cornwell, D. & Rawlinson, N., 2018. Constraints on North Anatolian fault zone width in the crust and upper mantle from S wave Teleseismic tomography, *J. geophys. Res.: Solid Earth,* **123,** 2908–2922.

Papaleo, E., Cornwell, D.G. & Rawlinson, N., 2017. Seismic tomography of the North Anatolian Fault: new insights into structural heterogeneity along a continental strike-slip fault, *Geophys. Res. Lett.,* **44,** doi:10.1002/2017GL072726.

Paul, A., Karabulut, H., Mutlu, A.K. & Salaün, G., 2014. A comprehensive and densely sampled map of shear-wave azimuthal anisotropy in the Aegean–Anatolia region, *Earth planet. Sci. Lett.,* **389,** 14–22.

Peng, Z. & Ben-Zion, Y., 2004. Systematic analysis of crustal anisotropy along the Karadere—Düzce branch of the North Anatolian fault, *Geophys. J. Int.,* **159,** 253–274.

Platt, J.P. & Behr, W.M., 2011. Deep structure of lithospheric fault zones, *Geophys. Res. Lett.,* **38,** L24308, doi:10.1029/2011GL049719.

Polat, G., Özel, N.M. & Koulakov, I., 2016. Investigating P- and S-wave velocity structure beneath the Marmara region (Turkey) and the surrounding area from local earthquake tomography, *Earth Planets Space,* **68,** 132.

Poyraz, S.A. *et al.*, 2015. New constraints on micro-seismicity and stress state in the western part of the North Anatolian Fault Zone: observations from a dense seismic array, *Tectonophysics,* **656,** 190–201.

Reilinger, R. *et al.*, 2006. GPS constraints on continental deformation in the Africa-Arabia-Eurasia continental collision zone and implications for the dynamics of plate interactions, *J. geophys. Res.: Solid Earth,* **111,** B05411, doi:10.1029/2005JB004051.

Rondenay, S., 2009. Upper mantle imaging with array recordings of converted and scattered teleseismic waves, *Surv. Geophys.,* **30,** 377–405.

Salaün, G. *et al.*, 2012. High-resolution surface wave tomography beneath the Aegean-Anatolia region: constraints on upper-mantle structure, *Geophys. J. Int.,* **190,** 406–420.

Sandvol, E., Seber, D., Barazangi, M., Vernon, F., Mellors, R. & Al-Amri, A., 1998. Lithospheric seismic velocity discontinuities beneath the Arabian Shield, *Geophys. Res. Lett.,* **25,** 2873–2876.

Schiffer, C., Jacobsen, B.H., Balling, N., Ebbing, J. & Nielsen, S.B., 2015. The East Greenland Caledonides—teleseismic signature, gravity and isostasy, *Geophys. J. Int.,* **203,** 1400–1418.

Schiffer, C., Stephenson, R., Oakey, G.N. & Jacobsen, B.H., 2016. The crustal structure of Ellesmere Island, Arctic Canada—teleseismic mapping across a remote intraplate orogenic belt, *Geophys. J. Int.,* **204,** 1579–1600.

Schildgen, T.F., Yıldırım, C., Cosentino, D. & Strecker, M.R., 2014. Linking slab break-off, Hellenic trench retreat, and uplift of the Central and Eastern Anatolian plateaus, *Earth-Sci. Rev.,* **128,** 147–168.

Storti, F., Holdsworth, R.E. & Salvini, F., 2003. Intraplate strike-slip deformation belts, *Geol. Soc. Lond., Spec. Publ.,* **210,** 1–14.

Svenningsen, L. & Jacobsen, B.H., 2007. Absolute S-velocity estimation from receiver functions, *Geophys. J. Int.,* **170,** 1089–1094.

Şengör, A.M.C., Tüysüz, O., İmren, C., Sakınç, M., Eyidoğan, H., Görür, N., Pichon, X.L. & Rangin, C., 2005. The North anatolian fault: a new look, *Ann. Rev. Earth planet. Sci.,* **33,** 37–112.

Şengör, A.M. & Yılmaz, Y., 1981. Tethyan evolution of Turkey: a plate tectonci approach. Tectonophysics, *Tectonophysics,* **75**(3-4), 181–241, doi: 10.1016/0040-1951(81)90275-4.

Tarantola, A. & Valette, B., 1982. Generalized nonlinear inverse problems solved using the least squares criterion, *Rev. Geophys.,* **20,** 219–232.

Taylor, G., Rost, S. & Houseman, G., 2016. Crustal imaging across the North Anatolian Fault Zone from the autocorrelation of ambient seismic noise, *Geophys. Res. Lett.,* **43,** doi:10.1002/2016GL067715.

Taymaz, T., Jackson, J. & McKenzie, D., 1991. Active tectonics of the north and central Aegean Sea, *Geophys. J. Int.,* **106,** 433–490.

Taymaz, T., Kasahara, J., Hirn, A. & Sato, T., 2001. Investigations of microearthquake activity within the Sea of Marmara and surrounding regions by using ocean bottom seismometers (OBS) and land seismographs: initial results, in *Presented at the Scientific Activities 2001 Symposia - Extended Abstracts,* May 8, 2001, ATLAS DBR-Offset Printing House, Istanbul Technical University, Faculty of Mines, pp. 42–51.

Taymaz, T., Wright, T.J., Yolsal, S., Tan, O., Fielding, E. & Seyitoğlu, G., 2007a. Source characteristics of the 6 June 2000 Orta–Çankırı (central Turkey) earthquake: a synthesis of seismological, geological and geodetic (InSAR) observations, and internal deformation of the Anatolian plate, *Geol. Soc. Lond. Spec. Publ.,* **291,** 259–290.

Taymaz, T., Yilmaz, Y. & Dilek, Y., 2007b. The geodynamics of the Aegean and Anatolia: introduction, *Geol. Soc. Lond., Spec. Publ.,* **291,** 1–16.

Vanacore, E.A., Taymaz, T. & Saygin, E., 2013. Moho structure of the Anatolian Plate from receiver function analysis, *Geophys. J. Int.,* **193,** 329–337.

Warren, L.M., Beck, S.L., Biryol, C.B., Zandt, G., Özacar, A.A. & Yang, Y., 2013. Crustal velocity structure of Central and Eastern Turkey from ambient noise tomography, *Geophys. J. Int.,* **194,** 1941–1954.

Weber, M. *et al.*, 2004. The crustal structure of the Dead Sea Transform, *Geophys. J. Int.,* **156,** 655–681.

Wiechert, E. & Zoeppritz, K., 1907. Ueber erdbebenwellen, *Nachrichten Von Ges. Wiss. Zu Gött. Math.-Phys. Kl.,* **1907,** 415.

Wilson, M., Neumann, E.-R., Davies, G.R., Timmerman, M.J., Heeremans, M. & Larsen, B.T., 2004. Permo-Carboniferous magmatism and rifting in Europe: introduction, *Geol. Soc. Lond. Spec. Publ.,* **223,** 1–10.

Yolsal-Çevikbilen, S., Biryol, C.B., Beck, S., Zandt, G., Taymaz, T., Adıyaman, H.E. & Özacar, A.A., 2012. 3-D crustal structure along the North Anatolian Fault Zone in north-central Anatolia revealed by local earthquake tomography, *Geophys. J. Int.,* **188,** 819–849.

Zhao, D., 2015. *Multiscale Seismic Tomography,* Springer.

Zhu, L., 2000. Crustal structure across the San Andreas Fault, southern California from teleseismic converted waves, *Earth planet. Sci. Lett.,* **179,** 183–190.

SUPPORTING INFORMATION

Supplementary data are available at *GJI* online.

Supplementary File S1. Receiver function and Vs_{app} of disregarded station DOGL. Consult caption of Fig. 3 for details.
Supplementary File S2. Table with detailed event data.
Supplementary File S3. Receiver function and Vs_{app}-curves of all used stations. Consult caption of Fig. 3 for details.
Supplementary File S4. Inversions of all used stations. Consult caption of Fig. 4 for details.
Supplementary File S5. Synthetic tests
Supplementary File S6. Inversion results of all used stations. Consult caption of Fig. 5 for details.
Supplementary File S7. Uncertainties, errors and data misfit

Please note: Oxford University Press is not responsible for the content or functionality of any supporting materials supplied by the authors. Any queries (other than missing material) should be directed to the corresponding author for the paper.